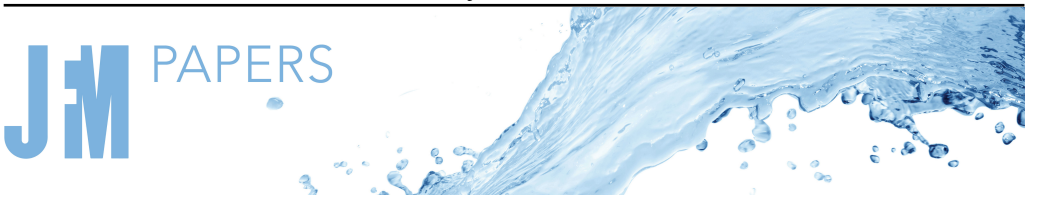
J. Fluid Mech. (2025), *vol.* 1020, A50, doi:10.1017/jfm.2025.10635



Broadband water wave reflector with customisable frequency range enabled by floating metaplates

He Liu[1], **Mohamed Farhat**[1], **Hakan Bagci**[1], **Sebastien Guenneau**[2,3] **and Ying Wu**[1]

[1]Computer, Electrical and Mathematical Science and Engineering (CEMSE) Division, King Abdullah University of Science and Technology (KAUST), Thuwal 23955-6900, Saudi Arabia

[2]UMI 2004 Abraham de Moivre-CNRS, Imperial College London, London SW7 2AZ, UK

[3]The Blackett Laboratory, Department of Physics, Imperial College London, London SW7 2AZ, UK

Corresponding authors: Ying Wu, ying.wu@kaust.edu.sa; Sebastien Guenneau, s.guenneau@imperial.ac.uk

(Received 25 March 2025; revised 4 July 2025; accepted 20 August 2025)

Research on water wave metamaterials based on local resonance has advanced rapidly. However, their application to floating structures for controlling surface gravity waves remains underexplored. In this work, we introduce the floating metaplate, a periodic array of resonators on a floating plate that leverages locally resonant bandgaps to effectively manipulate surface gravity waves. We employ the eigenfunction matching method combined with Bloch's theorem to solve the wave–structure interaction problem and obtain the band structure of the floating metaplate. An effective model based on averaging is developed, which agrees well with the results of numerical simulation, elucidating the mechanism of bandgap formation. Both frequency- and time-domain simulations demonstrate the floating metaplate's strong wave attenuation capabilities. Furthermore, by incorporating a gradient in the resonant frequencies of the resonators, we achieve the rainbow trapping effect, where waves of different frequencies are reflected at distinct locations. This enables the design of a broadband wave reflector with a tuneable operation frequency range. Our findings may lead to promising applications in coastal protection, wave energy harvesting and the design of resilient offshore renewable energy systems.

Key words: wave-structure interactions, surface gravity waves, wave scattering

© The Author(s), 2025. Published by Cambridge University Press. This is an Open Access article, distributed under the terms of the Creative Commons Attribution licence (https://creativecommons.org/licenses/by/4.0/), which permits unrestricted re-use, distribution and reproduction, provided the original article is properly cited.

https://doi.org/10.1017/jfm.2025.10635 Published online by Cambridge University Press

1. Introduction

The study of floating plates interacting with surface gravity waves has a long and rich history, driven by its importance to fundamental fluid mechanics and practical applications such as ocean engineering, wave energy conversion and coastal protection (Lamb 1997; Meylan 1997; Balmforth & Craster 1999; Meylan 2002; Zhang & Schreier 2022). Floating plates, often serving as simplified models for ice floes, very large floating structures and engineered platforms, play a crucial role in advancing our understanding of wave–structure interactions across various contexts. Recently, significant attention was directed toward leveraging plate arrays and other floating plate-based structures for manipulating water waves. For instance, Porter (2019) investigated the propagation of water waves through a periodic rectangular array of floating plates, highlighting its potential for wave attenuation. Wilks, Montiel & Wakes (2022) and Liang, Porter & Zheng (2024) demonstrated that graded arrays of surface-piercing vertical barriers (or plates) can effectively achieve the water wave rainbow trapping effect and broadband wave reflection, respectively. Loukogeorgaki & Kashiwagi (2019) proposed a type of concentric annular floating elastic plate to minimise wave drift forces. Subsequently, Iida, Zareei & Alam (2023) discovered that the same kind of annular floating composite plate could achieve omnidirectional cylindrical cloaking for deep-water waves. More recently, Michele *et al.* (2024*b*) explored rigid compound rectangular floating plates acting as efficient wave energy converters. These findings underscore the versatility of plate-based floating structures in controlling water waves.

On the other hand, over the past two decades, the use of phononic crystals and metamaterials for manipulating acoustic and elastic waves has received tremendous attention thanks to the exotic and extraordinary dynamic properties of these engineered structures (Ma & Sheng 2016; Craster *et al.* 2023). In particular, the locally resonant metamaterials (Liu *et al.* 2000, Zhou & Hu 2009; Zhou & Hu 2009), characterised by their sub-wavelength periodic structures and low-frequency bandgaps, have spurred significant advancements in areas such as vibration isolation, noise suppression and energy harvesting (one can refer to Wu *et al.* 2021). Moreover, the success of local resonance mechanisms in classical wave control has inspired researchers to explore analogous approaches for water wave manipulation, leading to the burgeoning development of water wave metamaterials based on local resonance (Zhu *et al.* 2024). For instance, Hu *et al.* (2011) demonstrated that periodic arrays of bottom-mounted tubes in water, leveraging low-frequency resonant bandgaps, can strongly block water waves; De Vita *et al.* (2021) studied the arrays of submerged harmonic oscillators designed to absorb wave energy, demonstrating significant attenuation when the wave and resonator frequencies are close. Subsequently, Lorenzo *et al.* (2023) experimentally investigated an array of submerged inverted cylindrical pendula, confirming the practical effectiveness of such configurations in mitigating surface gravity waves. More recently, Euvé *et al.* (2023) numerically and experimentally (Euvé *et al.* 2024) proposed a type of subwavelength resonant media supporting negative refraction of water waves; Zeng *et al.* (2023) and Zhang *et al.* (2024) demonstrated that floating periodic rigid resonators offer an efficient and straightforward approach to attenuating water waves.

Despite these advancements, the application of locally resonant metamaterials to control surface gravity waves, the most prevalent wave type in oceanic and coastal environments, remains less explored. Locally resonant metamaterial plates exhibit extraordinary performance in manipulating elastic waves and harvesting vibrational energy (Rupin *et al.* 2014; Miranda *et al.* 2020; Sugino, Ruzzene & Erturk 2020; Jin *et al.* 2021), nevertheless, their application in controlling surface gravity waves within the extensively

https://doi.org/10.1017/jfm.2025.10635 Published online by Cambridge University Press

studied field of floating plates is very limited. In this work, we investigate the wave–structure interaction problem involving floating metamaterial plates (also referred to as metaplates, see Wang *et al.* (2019)). We develop a fundamental computational framework for analysing the scattering of water waves by a floating metaplate and explore its potential applications in surface gravity wave control.

The proposed floating metaplate consists of a periodic arrangement of resonators mounted on a floating plate. As a proof-of-concept investigation, we focus on two-dimensional configurations, where one dimension of the plate is assumed to be infinitely large (Farhat *et al.* 2021; Michele *et al.* 2024*a*). The resonators are modelled as mass–spring systems, a widely adopted approach in the literature (Torrent, Mayou & Sánchez-Dehesa 2013; Gusev & Wright 2014; Chen, Hu & Huang 2017). We develop a numerical scheme for calculating the band structure of the periodic system. This scheme combines the eigenfunction matching method, well established for its high accuracy and reliability in solving wave scattering problems involving floating structures (Fox & Squire 1994; Molin 2001; Meylan 2019; Zheng *et al.* 2020; Iida *et al.* 2023), with Bloch's theorem, a foundational tool for analysing wave propagation in periodic structures (Chou 1998; Tokić & Yue 2019; McIver 2000). We study graded finite-size floating metaplates in both frequency- and time-domain, highlighting their exceptional potential for achieving the rainbow trapping effect in surface gravity waves and designing broadband water wave reflectors. Unlike previous studies, where graded structures were designed by modifying the overall configuration of submerged structures (Bennetts, Peter & Craster 2018) or adjusting the spacing between the barriers piercing into water (Archer *et al.* 2020; Wilks *et al.* 2022), our designed graded rainbow trapping structure relies on varying the resonant frequencies of the resonators on the floating plate, making it more feasible for deep-sea applications in ocean engineering.

This paper is organised as follows. The mathematical model and numerical scheme for an infinite periodic floating metaplate are outlined in § 2. Band structure analysis, using both the analytical model and the numerical scheme, is carried out in § 3. The frequency-domain response together with time-dependent solutions for a finite-size floating metaplate are illustrated in § 4. The rainbow trapping effect for the surface water wave and the broadband wave reflector enabled by graded floating metaplates are discussed in § 5. A conclusion is drawn in § 6.

2. A periodic floating metaplate

2.1. *Governing equation and boundary conditions*

We consider a thin elastic plate floating atop water. As illustrated in figure 1, the upper surface of the plate is periodically attached with resonators, forming the so-called floating metaplate. The plate is always in contact with the water surface and is thin enough such that Kirchhoff's thin plate theory is valid. We consider a Cartesian coordinate system with the x-axis coinciding with the water surface and the positive z-axis pointing upward. We assume that the fluid is incompressible, homogeneous and inviscid, and the flow is irrotational. Under these assumptions, the linear potential theory is adopted. The velocity potential $\Phi(x, t)$ takes the form of the following Laplace equation (Fox & Squire 1994):

$$\nabla^2\Phi = 0 \quad -H \leqslant z \leqslant 0, \tag{2.1}$$

where H is the depth of water. The seabed (no flow) boundary condition is given by

$$\frac{\partial\Phi}{\partial z} = 0 \quad z = -H, -\infty < x < \infty. \tag{2.2}$$

https://doi.org/10.1017/jfm.2025.10635 Published online by Cambridge University Press

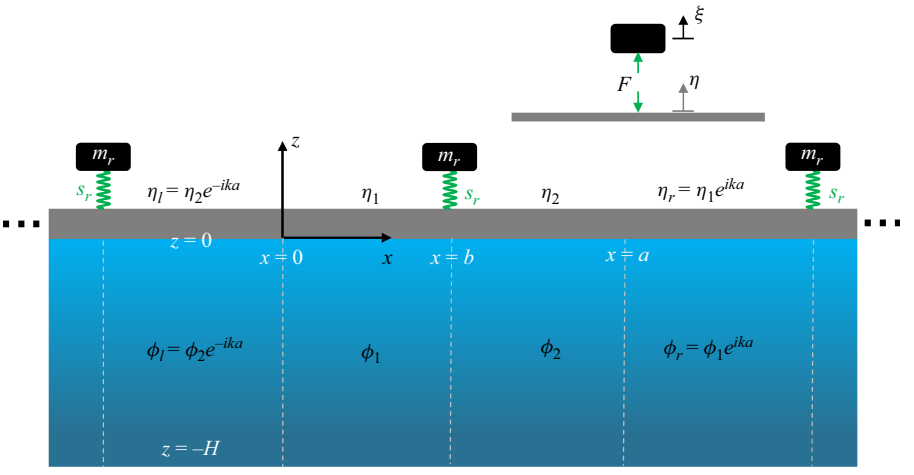


Figure 1. Schematic diagram of a floating plate, with periodic resonators attached on its surface, forming the so-called floating metaplate. The plate is assumed thin and elastic. One unit cell spans from $x = 0$ to $x = a$, in which the resonator is attached at $x = b$. The velocity potential of the water wave and the deflection of the plate are labelled by ϕ and η, respectively. The inset depicts the force diagram related to the interaction between the resonator and the plate.

The dynamic condition for the free surface reads

$$\frac{\partial \Phi}{\partial t} + gw = 0 \quad z = 0, \tag{2.3}$$

while that on the surface covered with the thin plate is

$$D\frac{\partial^4 w}{\partial x^4} + \rho_p h \frac{\partial^2 w}{\partial t^2} = p \quad z = 0, \tag{2.4}$$

where g is the acceleration due to gravity, $w(x, t)$ is the displacement of the fluid surface (which is also the vertical displacement of the plate), $D = Eh^3/12(1 - \nu^2)$ represents the flexural rigidity, with E, ν, h and ρ_p being the Young's modulus, Poisson's ratio, thickness and density of the plate, respectively. The surface pressure p in (2.4) satisfies

$$\rho\frac{\partial \Phi}{\partial t} + \rho g w + p = 0, \tag{2.5}$$

where ρ is the density of water. It should be pointed out that the effect of the resonator is embodied in boundary conditions to be described below, but not in the governing equation (2.4). In addition, the kinematic boundary condition reads

$$\frac{\partial \Phi}{\partial z} = \frac{\partial w}{\partial t} \quad z = 0. \tag{2.6}$$

Assuming that all motions are time-harmonic with angular frequency ω, the velocity potential of water waves Φ and the displacement of the plate w can be expressed as

$$\Phi(x, z, t) = \mathrm{Re}\left\{\phi(x, z)\mathrm{e}^{-\mathrm{i}\omega t}\right\}, \tag{2.7a}$$

$$w(x, t) = \mathrm{Re}\left\{\eta(x)\mathrm{e}^{-\mathrm{i}\omega t}\right\}, \tag{2.7b}$$

where the reduced velocity potential ϕ and plate deflection η are both complex valued.

https://doi.org/10.1017/jfm.2025.10635 Published online by Cambridge University Press

From (2.1)–(2.7), we can get the following boundary value problem in the frequency domain:

$$\frac{\partial^2\phi}{\partial x^2}+\frac{\partial^2\phi}{\partial z^2}=0 \quad -H\leqslant z<0, \tag{2.8a}$$

$$\frac{\partial\phi}{\partial z}=0 \quad z=-H, \tag{2.8b}$$

together with the boundary conditions at $z=0$, for the free surface, written as

$$\frac{\partial\phi}{\partial z}=\alpha\phi \quad z=0, \tag{2.9}$$

and for the surface covered with the plate as

$$\left(\beta\frac{\partial^4}{\partial x^4}+1-\alpha\gamma_0\right)\frac{\partial\phi}{\partial z}=\alpha\phi \quad z=0, \tag{2.10}$$

where α, β and γ_0 are

$$\alpha=\frac{\omega^2}{g},\ \beta=\frac{D}{\rho g},\ \gamma_0=\frac{\rho_p h}{\rho}, \tag{2.11}$$

respectively. Note that β and γ_0, which represent the bending stiffness term and inertia term, are two key parameters to characterise the physical properties of the plate.

2.2. *Eigenfunction matching method and Bloch's theorem*

We derive the solution by the eigenfunction matching method (Fox & Squire 1994). Using separation of variables, we can write the general solution to the velocity potential $\phi(x,z)$ as

$$\phi(x,z)=\sum_{n=0}^{N}X_n(x)\varphi_n(z) \quad \text{under the free surface,} \tag{2.12}$$

or

$$\phi(x,z)=\sum_{m=-2}^{M}Z_m(x)\psi_m(z) \quad \text{under the plate,} \tag{2.13}$$

where $\varphi_n(z)$ and $\psi_m(z)$ correspond to the normalised vertical eigenfunction of the potential under the free surface and the plate region, respectively, and can be expressed as

$$\varphi_n(z)=\frac{\cos\vartheta_n(z+H)}{\cos\vartheta_n H} \quad n\geqslant 0, \tag{2.14}$$

$$\psi_m(z)=\frac{\cos\kappa_m(z+H)}{\cos\kappa_m H} \quad m\geqslant -2, \tag{2.15}$$

in which the separation constant ϑ_n and κ_m are solutions of the following two dispersion equations, respectively:

$$\vartheta\tan(\vartheta H)=-\alpha \quad \text{under the free surface,} \tag{2.16}$$

$$\kappa\tan\kappa H=\frac{-\alpha}{\beta\kappa^4+1-\gamma_0\alpha} \quad \text{under the plate.} \tag{2.17}$$

https://doi.org/10.1017/jfm.2025.10635 Published online by Cambridge University Press

Note that the solutions of (2.16) are ϑ_0, which is a purely negative imaginary number, and ϑ_n ($n \geqslant 1$) which is a positive real number. While the solutions of (2.17) are κ_m ($m \geqslant -2$), in which κ_{-2} and κ_{-1} are complex with positive real parts, κ_0 is purely negative imaginary, and κ_m ($m \geqslant 1$) is purely positive real. Then, we can write $X_n(x)$ under the free surface in (2.12) and $Z_m(x)$ under the plate in (2.13) as

$$X_n(x) = l_n \mathrm{e}^{\vartheta_n x} + r_n \mathrm{e}^{-\vartheta_n x}, \tag{2.18}$$

and

$$Z_m(x) = a_m \mathrm{e}^{\kappa_m x} + b_m \mathrm{e}^{-\kappa_m x}, \tag{2.19}$$

respectively, where l_n, r_n ($n = 0, 1, 2, \ldots, N$) and a_m, b_m ($m = -2, -1, 0, \ldots, M$) are undetermined coefficients. It is worth noting that, while there are an infinite number of vertical modes (i.e. $\varphi(z)$ and $\psi(z)$), we truncate (2.12) and (2.13) at the Nth and Mth modes for numerical solutions.

From the kinematic boundary condition (2.6) and using (2.10), (2.13), (2.15) and (2.19), the deflection of the plate can be obtained as

$$\eta(x) = \frac{1}{-\mathrm{i}\omega} \frac{\partial \phi}{\partial z}\Big|_{z=0} = \sum_{m=-2}^{M} \frac{\mathrm{i}}{\omega} \frac{\alpha}{\beta \kappa_m^4 + 1 - \gamma_0 \alpha} \left(a_m \mathrm{e}^{\kappa_m x} + b_m \mathrm{e}^{-\kappa_m x}\right). \tag{2.20}$$

Since the resonators are periodically arranged on the floating plate with periodicity a in the x direction, it is possible to confine attention to one unit cell ranging from $x = 0$ to $x = a$ that contains only a single resonator, as shown in figure 2(a). Bloch's theorem states that, under a discrete lattice translation na ($n \in \mathbb{Z}$), any physical field, e.g. the velocity potential $\phi(x, z)$ or the plate deflection $\eta(x)$, can be obtained from the one within this unit cell being modulated by a plane wave (see Chou 1998), i.e.

$$\phi(x + na, z) = \phi(x, z)\mathrm{e}^{\mathrm{i}kna}, \ \ \eta(x + na) = \eta(x)\mathrm{e}^{\mathrm{i}kna}, \tag{2.21}$$

where k is the Bloch wavenumber.

We segment the unit cell at the point $x = b$ where the resonator is located, and express the velocity potential underneath the two segments (see figure 1) as

$$\phi_1(x, z) = \sum_{m=-2}^{M} \left(a_m \mathrm{e}^{\kappa_m x} + b_m \mathrm{e}^{-\kappa_m x}\right) \psi_m(z) \quad 0 \leqslant x \leqslant b, \tag{2.22a}$$

$$\phi_2(x, z) = \sum_{m=-2}^{M} \left(c_m \mathrm{e}^{\kappa_m x} + d_m \mathrm{e}^{-\kappa_m x}\right) \psi_m(z) \quad b \leqslant x \leqslant a, \tag{2.22b}$$

where κ_m is the mth root of (2.17) and a_m, b_m, c_m and d_m are undetermined coefficients. According to (2.21), we can write out the velocity potential that belongs to the left (i.e. $x < 0$) and right (i.e. $x > a$) segments adjacent to this unit cell as

$$\phi_l(x - a, z) = \phi_2(x, z)\mathrm{e}^{-\mathrm{i}ka} \quad b \leqslant x \leqslant a, \tag{2.23a}$$

$$\phi_r(x + a, z) = \phi_1(x, z)\mathrm{e}^{\mathrm{i}ka} \quad 0 \leqslant x \leqslant b. \tag{2.23b}$$

https://doi.org/10.1017/jfm.2025.10635 Published online by Cambridge University Press

From (2.20) and applying Bloch's theorem again, the deflection of the plate that belongs to distinct segments (see figure 1) can be expressed as

$$\eta_1(x) = \sum_{m=-2}^{M} \frac{\mathrm{i}}{\omega} \frac{\alpha}{\beta\kappa_m^4 + 1 - \gamma_0\alpha} \left(a_m \mathrm{e}^{\kappa_m x} + b_m \mathrm{e}^{-\kappa_m x}\right) \quad 0 \leqslant x \leqslant b, \tag{2.24a}$$

$$\eta_2(x) = \sum_{m=-2}^{M} \frac{\mathrm{i}}{\omega} \frac{\alpha}{\beta\kappa_m^4 + 1 - \gamma_0\alpha} \left(c_m \mathrm{e}^{\kappa_m x} + d_m \mathrm{e}^{-\kappa_m x}\right) \quad b \leqslant x \leqslant a, \tag{2.24b}$$

$$\eta_l(x-a) = \eta_2(x)\mathrm{e}^{-\mathrm{i}ka} \quad b \leqslant x \leqslant a, \tag{2.24c}$$

$$\eta_r(x+a) = \eta_1(x)\mathrm{e}^{\mathrm{i}ka} \quad 0 \leqslant x \leqslant b. \tag{2.24d}$$

Identical spatial relations hold for other physical quantities such as the horizontal velocity of the fluid $\partial\phi/\partial x$, rotation angle $\partial\eta/\partial x$, bending moment $D\partial^2\eta/\partial x^2$ and shear force $-D\partial^3\eta/\partial x^3$ of the plate (Iida & Umazume 2020). It is worth noting that the wavenumbers k in (2.23) and (2.24) need only be considered between $-\pi/a \leqslant k \leqslant \pi/a$, which is the first Brillouin zone (BZ), as solutions with all other real values k can be obtained by adding or subtracting a multiple of $2\pi/a$.

2.3. *Generalised eigenvalue problem*

We seek non-trivial solutions of the unknown coefficients mentioned in the previous section by considering the matching conditions associated with the potential and the boundary conditions of the plate. Specifically, we solve for values of Bloch wavenumbers k for a given angular frequency ω.

For the unit cell we selected, we consider the matching conditions of the velocity potential and its normal derivative across the boundary between distinct regions separated by $x = 0$, $x = b$ and $x = a$. This gives

$$\phi_1(b, z) = \phi_2(b, z), \text{ i.e.,}$$
$$\sum_{m=-2}^{M} \left(a_m \mathrm{e}^{\kappa_m b} + b_m \mathrm{e}^{-\kappa_m b}\right)\psi_m(z) = \sum_{m=-2}^{M} \left(c_m \mathrm{e}^{\kappa_m b} + d_m \mathrm{e}^{-\kappa_m b}\right)\psi_m(z), \tag{2.25}$$

$$\phi_l(0, z) = \phi_1(0, z), \text{ i.e.,}$$
$$\sum_{m=-2}^{M} \left(c_m \mathrm{e}^{\kappa_m a} + d_m \mathrm{e}^{-\kappa_m a}\right)\psi_m(z)\mathrm{e}^{-\mathrm{i}ka} = \sum_{m=-2}^{M} (a_m + b_m)\psi_m(z), \tag{2.26}$$

and

$$\left.\frac{\partial\phi_1(x, z)}{\partial x}\right|_{x=b} = \left.\frac{\partial\phi_2(x, z)}{\partial x}\right|_{x=b}, \text{ i.e.,}$$
$$\sum_{m=-2}^{M} \kappa_m \left(a_m \mathrm{e}^{\kappa_m b} - b_m \mathrm{e}^{-\kappa_m b}\right)\psi_m(z) = \sum_{m=-2}^{M} \kappa_m \left(c_m \mathrm{e}^{\kappa_m b} - d_m \mathrm{e}^{-\kappa_m b}\right)\psi_m(z), \tag{2.27}$$

$$\left.\frac{\partial\phi_l(x, z)}{\partial x}\right|_{x=0} = \left.\frac{\partial\phi_1(x, z)}{\partial x}\right|_{x=0}, \text{ i.e.,}$$
$$\sum_{m=-2}^{M} \kappa_m \left(c_m \mathrm{e}^{\kappa_m a} - d_m \mathrm{e}^{-\kappa_m a}\right)\psi_m(z)\mathrm{e}^{-\mathrm{i}ka} = \sum_{m=-2}^{M} \kappa_m (a_m - b_m)\psi_m(z). \tag{2.28}$$

https://doi.org/10.1017/jfm.2025.10635 Published online by Cambridge University Press

It is worth noting that the matching conditions across the right boundary of the unit cell (i.e. $x = a$) are exactly equivalent to (2.26) and (2.28). Since these relations must hold at every depth z, we solve these equations by multiplying both sides of (2.25), (2.26), (2.27) and (2.28) by the vertical eigenfunction $\varphi_n(z)$ (see (2.14)) and integrating from $z = -H$ to $z = 0$ to obtain

$$\sum_{m=-2}^{M} \left(a_m \mathrm{e}^{\kappa_m b} + b_m \mathrm{e}^{-\kappa_m b}\right) P_{nm} = \sum_{m=-2}^{M} \left(c_m \mathrm{e}^{\kappa_m b} + d_m \mathrm{e}^{-\kappa_m b}\right) P_{nm}, \tag{2.29}$$

$$\sum_{m=-2}^{M} \left(c_m \mathrm{e}^{\kappa_m a} + d_m \mathrm{e}^{-\kappa_m a}\right) P_{nm} \mathrm{e}^{-\mathrm{i}ka} = \sum_{m=-2}^{M} (a_m + b_m) P_{nm}, \tag{2.30}$$

and

$$\sum_{m=-2}^{M} \kappa_m \left(a_m \mathrm{e}^{\kappa_m b} - b_m \mathrm{e}^{-\kappa_m b}\right) P_{nm} = \sum_{m=-2}^{M} \kappa_m \left(c_m \mathrm{e}^{\kappa_m b} - d_m \mathrm{e}^{-\kappa_m b}\right) P_{nm}, \tag{2.31}$$

$$\sum_{m=-2}^{M} \kappa_m \left(c_m \mathrm{e}^{\kappa_m a} - d_m \mathrm{e}^{-\kappa_m a}\right) P_{nm} \mathrm{e}^{-\mathrm{i}ka} = \sum_{m=-2}^{M} \kappa_m (a_m - b_m) P_{nm}, \tag{2.32}$$

where $0 \leqslant n \leqslant N$, and P_{nm} is the inner product of $\varphi_n(z)$ and $\psi_m(z)$ (Meylan 2019), i.e.

$$\begin{aligned} P_{nm} &= \int_{-H}^{0} \varphi_n(z)\psi_m(z)\mathrm{d}z \\ &= \frac{\vartheta_n \sin \vartheta_n H \cos \kappa_m H - \kappa_m \cos \vartheta_n H \sin \kappa_m H}{\cos \vartheta_n H \cos \kappa_m H (\vartheta_n^2 - \kappa_m^2)}. \end{aligned} \tag{2.33}$$

Note that the total number of equations contained in (2.29)–(2.32) is $4(N+1)$. It is also worth noting that, by taking advantage of the completeness, the vertical eigenfunctions $\varphi_n(z)$ of the free surface waves, instead of those $\psi_m(z)$ underneath the elastic plate, are selected for the projection operations (Kohout *et al.* 2007; Meng & Lu 2017).

Then we consider the matching and boundary conditions of the plate. At $x = 0$, the deflection, the rotation angle, the bending moment and the shear force are continuous, i.e.

$$\begin{aligned} \eta_l(0) = \eta_1(0), \text{ i.e., } &\sum_{m=-2}^{M} \frac{\mathrm{i}}{\omega} \frac{\alpha}{\beta\kappa_m^4 + 1 - \gamma_0\alpha} \left(c_m \mathrm{e}^{\kappa_m a} + d_m \mathrm{e}^{-\kappa_m a}\right) \mathrm{e}^{-\mathrm{i}ka} \\ &= \sum_{m=-2}^{M} \frac{\mathrm{i}}{\omega} \frac{\alpha}{\beta\kappa_m^4 + 1 - \gamma_0\alpha} (a_m + b_m), \end{aligned} \tag{2.34}$$

$$\begin{aligned} \left.\frac{\partial \eta_l}{\partial x}\right|_{x=0} = \left.\frac{\partial \eta_1}{\partial x}\right|_{x=0}, \text{ i.e., } &\sum_{m=-2}^{M} \frac{\mathrm{i}}{\omega} \frac{\alpha}{\beta\kappa_m^4 + 1 - \gamma_0\alpha} \kappa_m \left(c_m \mathrm{e}^{\kappa_m a} - d_m \mathrm{e}^{-\kappa_m a}\right) \mathrm{e}^{-\mathrm{i}ka} \\ &= \sum_{m=-2}^{M} \frac{\mathrm{i}}{\omega} \frac{\alpha}{\beta\kappa_m^4 + 1 - \gamma_0\alpha} \kappa_m (a_m - b_m), \end{aligned} \tag{2.35}$$

$$D \left.\frac{\partial^2 \eta_l}{\partial x^2}\right|_{x=0} = D \left.\frac{\partial^2 \eta_1}{\partial x^2}\right|_{x=0}, \text{ i.e., } \sum_{m=-2}^{M} \frac{\mathrm{i}}{\omega} \frac{\alpha}{\beta\kappa_m^4 + 1 - \gamma_0\alpha} \kappa_m^2 \left(c_m \mathrm{e}^{\kappa_m a} + d_m \mathrm{e}^{-\kappa_m a}\right) \mathrm{e}^{-\mathrm{i}ka}$$

https://doi.org/10.1017/jfm.2025.10635 Published online by Cambridge University Press

$$= \sum_{m=-2}^{M} \frac{\mathrm{i}}{\omega} \frac{\alpha}{\beta\kappa_m^4 + 1 - \gamma_0\alpha} \kappa_m^2 (a_m + b_m), \tag{2.36}$$

$$-D\frac{\partial^3 \eta_l}{\partial x^3}\Big|_{x=0} = -D\frac{\partial^3 \eta_1}{\partial x^3}\Big|_{x=0}, \text{ i.e., } \sum_{m=-2}^{M} \frac{\mathrm{i}}{\omega} \frac{\alpha}{\beta\kappa_m^4 + 1 - \gamma_0\alpha} \kappa_m^3 \left(c_m \mathrm{e}^{\kappa_m a} - d_m \mathrm{e}^{-\kappa_m a}\right) \mathrm{e}^{-\mathrm{i}ka}$$

$$= \sum_{m=-2}^{M} \frac{\mathrm{i}}{\omega} \frac{\alpha}{\beta\kappa_m^4 + 1 - \gamma_0\alpha} \kappa_m^3 (a_m - b_m). \tag{2.37}$$

Note that the continuity conditions at $x = a$ are equivalent to those at $x = 0$. Finally, at the point where the resonator is located ($x = b$), the deflection, the rotation angle and the bending moment are continuous, but there is a jump of F in the shear force, where F comes from the dynamic force in the spring of the resonator (see the inset in figure 1) and can be expressed as

$$F = s_r(\eta|_{x=b} - \Xi) = -m_r\omega^2\Xi, \tag{2.38}$$

where the assumption $\xi = \Xi \mathrm{e}^{-\mathrm{i}\omega t}$ was used, and s_r and m_r are the stiffness of the spring and the mass of the resonator, respectively. Note that the rightmost term in (2.38) arises from applying Newton's second law to the resonator. Equation (2.38) implies $\Xi = s_r\eta|_{x=b}/(s_r - m_r\omega^2)$, so we have

$$F = s_r\eta|_{x=b} \frac{-\tilde{\omega}^2}{1 - \tilde{\omega}^2}, \tag{2.39}$$

where $\tilde{\omega}$ is the normalised angular frequency by the natural frequency of the resonator ω_0, defined as

$$\tilde{\omega} = \frac{\omega}{\omega_0}, \ \omega_0 = \sqrt{\frac{s_r}{m_r}}. \tag{2.40}$$

Consequently, the matching conditions at $x = b$ read

$$\eta_1(b) = \eta_2(b), \text{ i.e., } \sum_{m=-2}^{M} \frac{\mathrm{i}}{\omega} \frac{\alpha}{\beta\kappa_m^4 + 1 - \gamma_0\alpha} \left(a_m \mathrm{e}^{\kappa_m b} + b_m \mathrm{e}^{-\kappa_m b}\right)$$

$$= \sum_{m=-2}^{M} \frac{\mathrm{i}}{\omega} \frac{\alpha}{\beta\kappa_m^4 + 1 - \gamma_0\alpha} \left(c_m \mathrm{e}^{\kappa_m b} + d_m \mathrm{e}^{-\kappa_m b}\right), \tag{2.41}$$

$$\frac{\partial \eta_1}{\partial x}\Big|_{x=b} = \frac{\partial \eta_2}{\partial x}\Big|_{x=b}, \text{ i.e., } \sum_{m=-2}^{M} \frac{\mathrm{i}}{\omega} \frac{\alpha}{\beta\kappa_m^4 + 1 - \gamma_0\alpha} \kappa_m \left(a_m \mathrm{e}^{\kappa_m b} - b_m \mathrm{e}^{-\kappa_m b}\right)$$

$$= \sum_{m=-2}^{M} \frac{\mathrm{i}}{\omega} \frac{\alpha}{\beta\kappa_m^4 + 1 - \gamma_0\alpha} \kappa_m \left(c_m \mathrm{e}^{\kappa_m b} - d_m \mathrm{e}^{-\kappa_m b}\right), \tag{2.42}$$

$$D\frac{\partial^2 \eta_1}{\partial x^2}\Big|_{x=b} = D\frac{\partial^2 \eta_2}{\partial x^2}\Big|_{x=b}, \text{ i.e., } \sum_{m=-2}^{M} \frac{\mathrm{i}}{\omega} \frac{\alpha}{\beta\kappa_m^4 + 1 - \gamma_0\alpha} \kappa_m^2 \left(a_m \mathrm{e}^{\kappa_m b} + b_m \mathrm{e}^{-\kappa_m b}\right)$$

$$= \sum_{m=-2}^{M} \frac{\mathrm{i}}{\omega} \frac{\alpha}{\beta\kappa_m^4 + 1 - \gamma_0\alpha} \kappa_m^2 \left(c_m \mathrm{e}^{\kappa_m b} + d_m \mathrm{e}^{-\kappa_m b}\right), \tag{2.43}$$

https://doi.org/10.1017/jfm.2025.10635 Published online by Cambridge University Press

$$D\frac{\partial^3\eta_1}{\partial x^3}\Big|_{x=b} - D\frac{\partial^3\eta_2}{\partial x^3}\Big|_{x=b} = F, \text{ i.e., } \sum_{m=-2}^{M} \frac{\mathrm{i}}{\omega}\frac{\alpha}{\beta\kappa_m^4 + 1 - \gamma_0\alpha} \times \left[\left(\kappa_m^3 + \frac{s_r}{D}\frac{\tilde{\omega}^2}{1-\tilde{\omega}^2}\right) a_m \mathrm{e}^{\kappa_m b} - \left(\kappa_m^3 - \frac{s_r}{D}\frac{\tilde{\omega}^2}{1-\tilde{\omega}^2}\right) b_m \mathrm{e}^{-\kappa_m b}\right] = \sum_{m=-2}^{M} \frac{\mathrm{i}}{\omega}\frac{\alpha}{\beta\kappa_m^4 + 1 - \gamma_0\alpha}\kappa_m^3\left(c_m \mathrm{e}^{\kappa_m b} - d_m \mathrm{e}^{-\kappa_m b}\right). \tag{2.44}$$

Combining (2.29)–(2.37) and (2.41)–(2.44), we have $4(N+3)$ equations and $4(M+3)$ unknowns in total. Letting $M = N$ and after some recombination, we get the following homogeneous equation:

$$\boldsymbol{K}\boldsymbol{x} = \boldsymbol{0}, \tag{2.45}$$

where $\boldsymbol{x}$ is the vector containing all the unknowns, i.e.

$$\boldsymbol{x} = [a_{-2}, a_{-1}, \ldots, a_M, b_{-2}, b_{-1}, \ldots, b_M, c_{-2}, c_{-1}, \ldots, c_M, d_{-2}, d_{-1}, \ldots, d_M]^{\mathrm{T}}, \tag{2.46}$$

and $\boldsymbol{K}$ is the coefficient matrix, written as

$$\boldsymbol{K}(\omega) = \begin{bmatrix} \boldsymbol{\mathcal{A}}(\omega) & \mathrm{e}^{-\mathrm{i}ka}\boldsymbol{\mathcal{B}}(\omega) \\ \boldsymbol{\mathcal{C}}(\omega) & \boldsymbol{\mathcal{D}}(\omega) \end{bmatrix}_{4(M+3)\times 4(M+3)}, \tag{2.47}$$

where submatrices $\boldsymbol{\mathcal{A}}$, $\boldsymbol{\mathcal{B}}$, $\boldsymbol{\mathcal{C}}$ and $\boldsymbol{\mathcal{D}}$ can be found in Appendix A.

The condition of non-zero solutions requires $\mathrm{Det}[\boldsymbol{K}] = 0$, which reduces to the following generalised eigenvalue problem

$$\mathrm{Det}[\boldsymbol{\mathcal{D}}(\omega) - \lambda\boldsymbol{\mathcal{M}}(\omega)] = 0, \tag{2.48}$$

where $\lambda = \mathrm{e}^{-\mathrm{i}ka}$ and $\mathcal{M}(\omega) = \boldsymbol{\mathcal{C}}\boldsymbol{\mathcal{A}}^{-1}\boldsymbol{\mathcal{B}}$. For any given angular frequency ω, we can solve for eigenvalues λ, and the non-trivial solutions which represent the propagating waves correspond to the real values of k such that $|\lambda| = 1$. This results in the dispersion relation $\omega(k)$ of the periodic floating metaplate.

3. Band structure analysis of the floating metaplate

In addition to the numerical method described above, we present a simple analytical model to derive the dispersion relation and utilise it to elucidate the mechanism underlying the bandgap. The results obtained from this model are compared with those calculated from the numerical method. The applicable condition for the analytical model is also discussed in the following.

3.1. *Analytical model: uniform floating plate with effective medium*

We refer to the model solved by the aforementioned numerical method as the real model, shown in figure 2(*a*), in which each unit cell contains a single spring–mass resonator. Its equivalent model is illustrated in figure 2(*b*), where a uniformly distributed spring–mass layer across the unit cell is used to replace the single resonator in the unit cell of the real model. It is ensured that the total mass and the total stiffness of the distributed spring–mass layer in the equivalent model are identical to those of the resonator in the real model. The underlying mathematical principle of this approximation is the use of a rectangular pulse of width a to approximate the δ-function within one unit cell (Haberman 2013). After this

https://doi.org/10.1017/jfm.2025.10635 Published online by Cambridge University Press

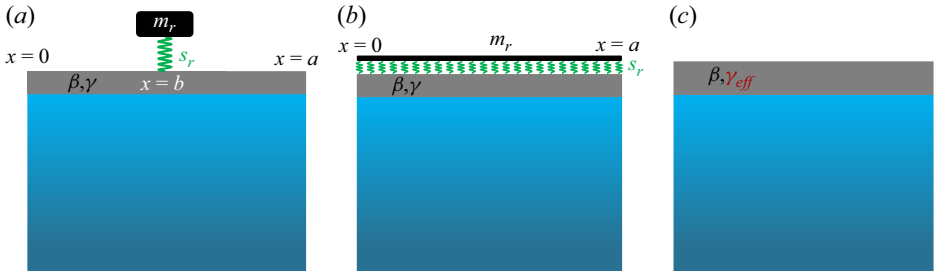


Figure 2. (*a*) One unit cell of the real model, i.e. floating plate attached with a resonator at a discrete position. (*b*) The same unit cell of the equivalent model, where the discrete resonator is modelled by uniformly distributed masses and springs. (*c*) The effective model, with the effective parameter γ_{eff} descried by (3.8).

discrete-to-continuous approximation, (2.4) should be modified as

$$D\frac{\partial^4 w}{\partial x^4} + \rho_p h\frac{\partial^2 w}{\partial t^2} = p + \frac{s_r}{a}(\tilde{w} - w) \quad z = 0, \tag{3.1}$$

where $\tilde{w}(x, t)$ represents the vertical displacement of the distributed mass layer. Note that the last term in (3.1) characterises the traction (or pressure) acting on the upper surface of the plate, which reflects Hooke's law. On the other hand, the governing equation with respect to the displacement $\tilde{w}(x, t)$ of the distributed mass layer reads

$$\frac{m_r}{a}\frac{\partial^2 \tilde{w}}{\partial t^2} = \frac{s_r}{a}(w - \tilde{w}), \tag{3.2}$$

which reflects Newton's second law. Assuming the harmonic solution, eliminating the term $\tilde{w}$ by substituting (3.2) into (3.1), and combining with (2.5) and (2.6), we get

$$\left\{ D\frac{\partial^4}{\partial x^4} + \rho g - \left[\frac{m_r}{a}\frac{1}{1 - \left(\frac{\omega}{\omega_0}\right)^2} + \rho_p h \right] \omega^2 \right\} \frac{\partial \phi}{\partial z} = \rho\omega^2 \phi, \tag{3.3}$$

where ω_0 can be found in (2.40). Plugging the basic solution $\phi(x, z) = \mathrm{e}^{\mathrm{i}kx}\cosh k(z + H)$, which satisfies (2.1) and boundary condition (2.2), into (3.3), we obtain the dispersion equation expressed as

$$\left\{ \beta k^4 + 1 - \left[\gamma_1 \frac{1}{1 - \left(\frac{\omega}{\omega_0}\right)^2} + \gamma_0 \right] \alpha \right\} k \tanh kH = \alpha, \tag{3.4}$$

where α, β and γ_0 are given in (2.11), and

$$\gamma_1 = \frac{m_r}{a\rho}. \tag{3.5}$$

Through (3.4) and (3.5), the dispersion relation $\omega(k)$ can be explicitly solved. For the sake of simplicity, it is listed in Appendix B.

Comparing (3.4) with the well-known dispersion equation for a bare plate floating atop water, which can be recast from (2.17) and written as (Fox & Squire 1994)

$$\left(\beta k^4 + 1 - \gamma_0\alpha\right) k \tanh kH = \alpha, \tag{3.6}$$

https://doi.org/10.1017/jfm.2025.10635 Published online by Cambridge University Press

Parameter	Description	Value
g	Acceleration due to gravity	$9.8\ \mathrm{m\ s^{-2}}$
H	Depth of water	10 m
ρ	Density of water	$1000\ \mathrm{kg\ m^{-3}}$
β	Bending stiffness term	$0.05\ \mathrm{m^4}$
γ_0	Mass density term	0.01 m
a	Periodicity of a unit cell	1 m
b	Location of the resonator	$0.5a$
m_r	Mass of the resonator	10 kg
ω_0	Resonant frequency of the resonator	$10\ \mathrm{rad\ s^{-1}}$
N	Truncation order in (2.12)	20
M	Truncation order in (2.13)	20

Table 1. Values of the relevant parameters for solving the problem.

one can immediately recognise that (3.4) is nothing but the dispersion equation for a floating plate with the same value of β but a modified γ_0 term, expressed as

$$\left(\beta k^4 + 1 - \gamma_{eff}\,\alpha\right) k \tanh kH = \alpha, \tag{3.7}$$

where

$$\gamma_{eff} = \gamma_1 \frac{1}{1 - \left(\frac{\omega}{\omega_0}\right)^2} + \gamma_0. \tag{3.8}$$

From this perspective, the floating metaplate shown in figure 2(a) can be regarded as a uniform floating plate, represented by the effective model displayed in figure 2(c), with the parameter β unchanged but γ_0 replaced by γ_{eff}. We can notice that γ_{eff} characterises the effective mass density of this effective-medium plate, embodying the inertia term of the original bare plate, i.e. γ_0, and an additional mass density term, i.e. γ_1, contributed from the resonator. This expression indicates that γ_{eff} of the effective plate is highly dependent on the ratio between the forcing frequency ω and the resonant frequency ω_0, closely resembling the effective dynamic mass defined in the literature on acoustic and elastic metamaterials (Huang, Sun & Huang 2009; Fedele, Suryanarayana & Yavari 2023). In the following, we show that the analytical dispersion relation (3.7), derived from this effective model, provides valuable insights into the band structure characteristics of such a complex system.

3.2. *Band structure analysis*

Unless otherwise specified, we will consider the values for the relevant parameters listed in table 1. Note that the values of β and γ_0 are chosen according to those reported earlier (e.g. Meylan 2019; Zheng *et al.* 2020; Iida *et al.* 2023).

We first examine the dispersion curve for a bare plate floating on the water surface. To numerically derive the dispersion relation $\omega(k)$, using the numerical scheme described in § 2, we set the spring stiffness of the resonator, s_r, to approach zero, causing the resonant frequency ω_0 to vanish. This limiting case of the metaplate exactly corresponds to a bare plate. In figure 3(a), we plot the dispersion curve as $s_r \to 0$, alongside the analytical dispersion relation for a floating bare plate given by (3.6). The results obtained from these two approaches exhibit excellent agreement, validating our numerical scheme.

https://doi.org/10.1017/jfm.2025.10635 Published online by Cambridge University Press

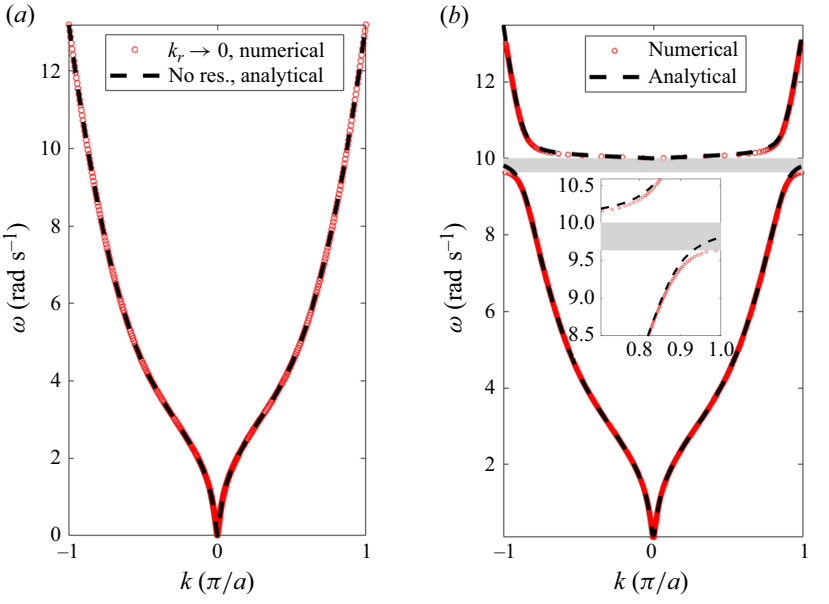


Figure 3. (*a*) Comparison of dispersion curve for a floating bare plate, obtained from numerical method and analytical formula. (*b*) Comparison of band structure for a floating metaplate, obtained from numerical method and analytical formulas enabled by the equivalent model shown in figure 2. The grey shading indicates the locally resonant bandgap obtained by numerical method. The inset shows a magnified view of the band structure at $k = \pi/a$.

Then we consider the floating metaplate with reasonably selected parameter values shown in table 1. The band structures obtained from the numerical method are plotted in figure 3(*b*), together with those obtained from the analytical model described by (3.7) and (3.8) (see Appendix B for the explicit expression of $\omega(k)$). It is evident that a bandgap forms between frequencies around 9.5–10 rad s^{-1}, highlighted in grey, close to the resonant frequency of the resonator, i.e. 10 rad s^{-1}. This bandgap is induced by the local resonance rather than the Bragg scattering. We draw this conclusion based on the following two considerations. First, for a periodic floating metaplate with periodicity a, the frequency at which a bandgap arises due to the Bragg scattering can be estimated using the condition $2\pi n/k = 2a$ ($n \in \mathbb{N}$) (Lorenzo *et al.* 2023), i.e.

$$\omega \approx \sqrt{g\frac{\beta k^5 + k}{\gamma_0 k + 1}}\bigg|_{k=\frac{n\pi}{a}}, \tag{3.9}$$

where the dispersion equation (3.6) has been used. For $n = 1$, the lowest Bragg bandgap occurs at around 13.2 rad s^{-1}, which is higher than the bandgap presented. Second, this bandgap exhibits the characteristic profile of a locally resonant bandgap (i.e. the lower bound of the bandgap is dictated by the lower branch of the dispersion curve which is flat at the first BZ edge $k = \pi/a$, while the upper bound is governed by the higher branch which is flat at the first BZ centre $k = 0$). In the following, we provide explanations of the resonance-induced bandgap obtained here by directly examining the behaviour as $\omega \to \omega_0$ in the original dispersion (3.4) (i.e. (3.7)), which can be fully expressed as

$$\left\{\beta k^4 + 1 - \left[\gamma_1 \frac{1}{1 - \left(\frac{\omega}{\omega_0}\right)^2} + \gamma_0\right]\frac{\omega^2}{g}\right\} k \tanh kH = \frac{\omega^2}{g}. \tag{3.10}$$

https://doi.org/10.1017/jfm.2025.10635 Published online by Cambridge University Press

On the one hand, if $\omega \to \omega_{0-}$, i.e. $\omega = \omega_0 - \Delta\omega$ where $\Delta\omega \to 0$, the term

$$\gamma_1 \frac{1}{1 - \left(\frac{\omega_0 - \Delta\omega}{\omega_0}\right)^2} \sim \frac{\gamma_1 \omega_0}{2\Delta\omega} \to \infty, \tag{3.11}$$

which dominates the terms in $[\cdot]$, then, the dispersion (3.10) can be approximated as

$$\left(\beta k^4 + 1 - \frac{\gamma_1 \omega_0^3}{2g\Delta\omega}\right) k \tanh kH = \frac{\omega_0^2}{g}. \tag{3.12}$$

Because the Bloch wavenumber k is confined within the first BZ (i.e. $k \in [-\pi/a, \pi/a]$), the term $\beta k^4 + 1$ is positive and bounded by $\beta(\pi/a)^4 + 1$. Since $k \tanh kH$ is non-negative, if $\beta(\pi/a)^4 + 1 < \gamma_1 \omega_0^3 / 2g\Delta\omega$, the left-hand side of (3.12) is non-positive, while its right-hand side is positive, indicating no real solutions can be found for (3.12). This means that when ω is smaller than but very close to ω_0, there is a bandgap.

On the other hand, if $\omega \to \omega_{0+}$, i.e. $\omega = \omega_0 + \Delta\omega$ where $\Delta\omega \to 0$, the term

$$\gamma_1 \frac{1}{1 - \left(\frac{\omega_0 + \Delta\omega}{\omega_0}\right)^2} \sim -\frac{\gamma_1 \omega_0}{2\Delta\omega} \to -\infty, \tag{3.13}$$

then, the dispersion (3.10) becomes

$$\left(\beta k^4 + 1 + \frac{\gamma_1 \omega_0^3}{2g\Delta\omega}\right) k \tanh kH = \frac{\omega_0^2}{g}. \tag{3.14}$$

Both sides of (3.14) are always positive if $k \neq 0$, indicating it is possible to find real solutions and therefore propagating bands exist when ω is slightly larger than ω_0.

When $\omega = \omega_0$, to make (3.10) valid, k must be zero. To check if $(\omega = \omega_0, k = 0)$ is a solution, we re-examine the expression of $\omega(k)$ derived from (3.4) (shown in Appendix B) and found that it is indeed a solution.

These findings are clearly manifested in the band structure shown in figure 3(*b*), where the bandgap occurs right below the resonator's natural frequency ω_0, and the dispersion branch above the bandgap starts from $(\omega = \omega_0, k = 0)$. These features will be the basis in the design a broadband water wave reflector with a customisable frequency range that will be discussed in § 5.

3.3. *Effect of key parameters on bandgap evolution*

To demonstrate the generality of the features revealed by the band structure analysis in § 3.2, we investigate how the bandgap evolves as several key physical parameters are varied. Specifically, we examine the influence of the normalised stiffness parameter β, the normalised mass term γ_1, the depth of the water H and the periodicity a of the metaplate on the location and width of the bandgap.

First, by varying β, the variation of the bandgap is shown in figure 4(*a*). It can be seen that the gap width decreases as β increases. Note that the bandgap's upper edge always occurs at $\omega_0 = 10\,\text{rad s}^{-1}$.

Second, we consider the variation of the parameter $\gamma_1 = m_r/a\rho$, which characterises the mass of the resonator. Increasing γ_1 means increasing the mass of the resonator m_r, and consequently decreasing the resonant frequency as $\omega_0 = \sqrt{s_r/m_r}$. This is shown in figure 4(*b*), where the upper edge of the bandgap, determined by ω_0, indeed decreases as γ_1 increases.

https://doi.org/10.1017/jfm.2025.10635 Published online by Cambridge University Press

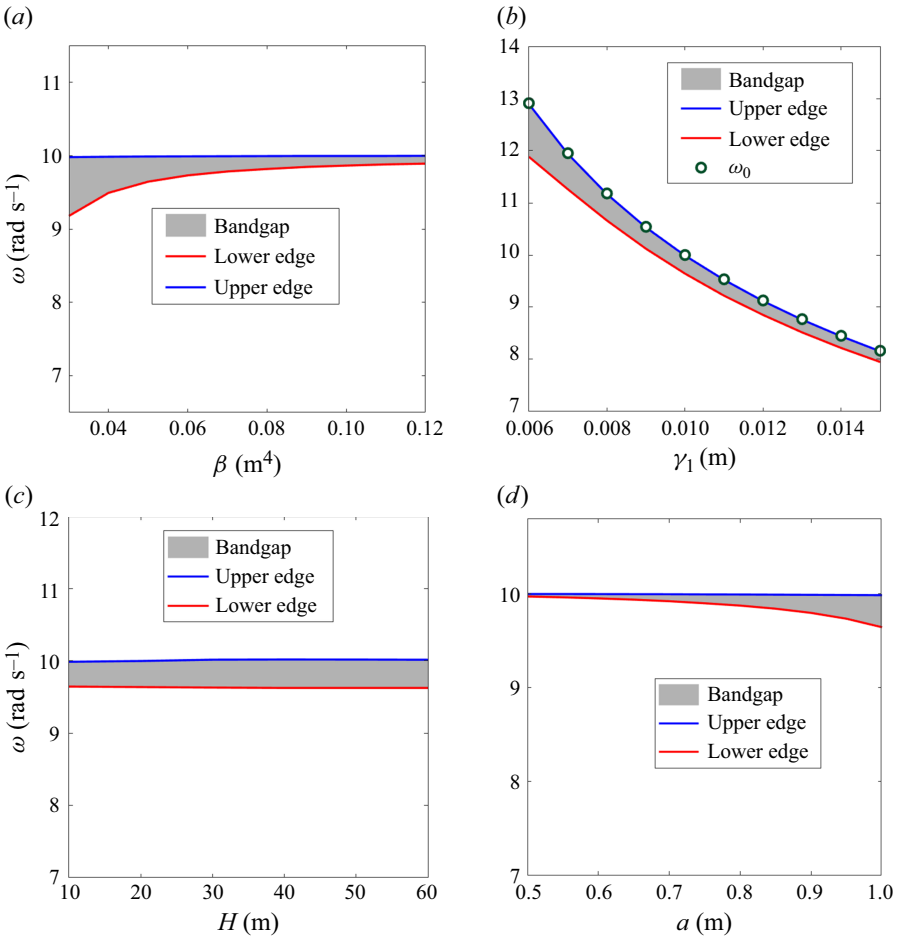


Figure 4. Evolution of the bandgap on varying parameters (*a*) β, (*b*) γ_1, (*c*) H and (*d*) a. The four figures were obtained by changing their respective parameters while keeping the other parameters unchanged as original ones taken in figure 3, where $\beta = 0.05$, $\gamma_1 = 0.01$, $H = 10$ and $a = 1$.

Third, we change H from its original value of 10 to 60 m, which means a deeper water region is considered. The variation of the bandgap is shown in figure 4(*c*), indicating that the bandgap is almost unchanged.

Last but not least, we change a from its original value of 1 to 0.5 m. The variation of the bandgap is shown in figure 4(*d*), indicating that the bandgap size decreases as the periodicity a decreases.

In a nutshell, although the frequency and the width of the bandgap may change when the parameters are altered, the overall features of the band structure of the decorated floating plate remain the same, i.e. there exists a resonance-induced bandgap located right below the resonant frequency ω_0.

3.4. *Error analysis and applicable criteria for the analytical model*

As shown in figure 3(*b*), the band structure derived from the simplified analytical model closely matches the numerical results across almost the entire wavenumber k range in the first BZ, with noticeable discrepancies only near the first BZ edge. We will provide an explanation for the origin of these discrepancies and give an brief error-analysis–based

https://doi.org/10.1017/jfm.2025.10635 Published online by Cambridge University Press

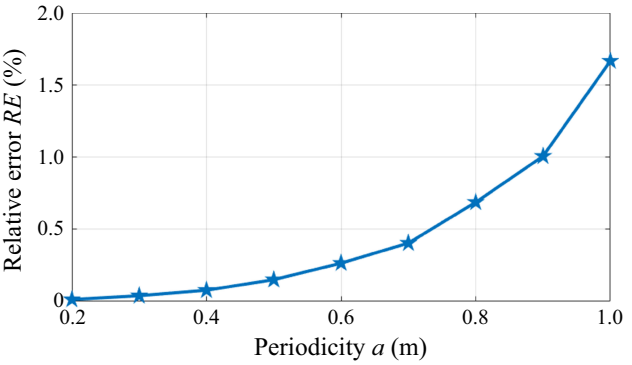


Figure 5. Variation of the relative error RE (3.15) between the frequency at $k = \pi/a$ from the two models with respect to the periodicity a.

discussion of when the analytical (equivalent) model remains reliably applicable, with a focus on the unit cell periodicity a.

It is worth emphasising that the analytical model is derived by replacing discrete resonators with uniformly distributed masses and springs (Chen *et al.* 2019), as shown in figure 2. Mathematically, this averaging process can be regarded as using a rectangular pulse function to approximate the Dirac delta function (Haberman 2013), which results in the discrepancies observed in the band structures obtained from analytical and numerical models. In this approximation, the rectangular pulse function better approximates the δ-function as a decreases, meaning the smaller the periodicity, the better the equivalent model. The discrepancies at large wave vectors stem from this approximation.

We define the relative error (RE) between the frequency at $k = \pi/a$ from the real model (numerical) and the equivalent model (analytical) as

$$RE = \frac{\left|\omega_{re}\left(\frac{\pi}{a}\right) - \omega_{eq}\left(\frac{\pi}{a}\right)\right|}{\omega_{re}\left(\frac{\pi}{a}\right)} \times 100\,\%, \tag{3.15}$$

where $\omega_{re}(\pi/a)$ denotes the low-branch frequency at π/a from the real model, while $\omega_{eq}(\pi/a)$ is that from the equivalent model (referring to the inset in figure 3(b) to clearly visualise the discrepancy between them).

We evaluate the relative error RE for various values of a while keeping all other parameters fixed as in table 1. Figure 5 presents the result, illustrating that, as the periodicity a decreases, the relative error between the two models diminishes. This indicates that the equivalent model can more accurately represent the real system when the unit cell size of the periodic floating metaplate is relatively small, in agreement with the conclusion derived above from mathematical viewpoint.

4. Frequency- and time-domain responses of a finite-size floating metaplate

We consider a finite-size floating metaplate consisting of N_c unit cells, as depicted in figure 6. We assume a monochromatic incident wave with unit elevation coming from the right, travelling along the negative x-direction.

4.1. *Frequency-domain analysis*

We can separate the region into three parts: free surface on the left-hand side for $x < 0$ (labelled by subscript 'l', with transmitted wave), plate-covered region for $0 < x < N_c a$ (labelled by subscript 'c', with gravity flexural wave) and free surface on

https://doi.org/10.1017/jfm.2025.10635 Published online by Cambridge University Press

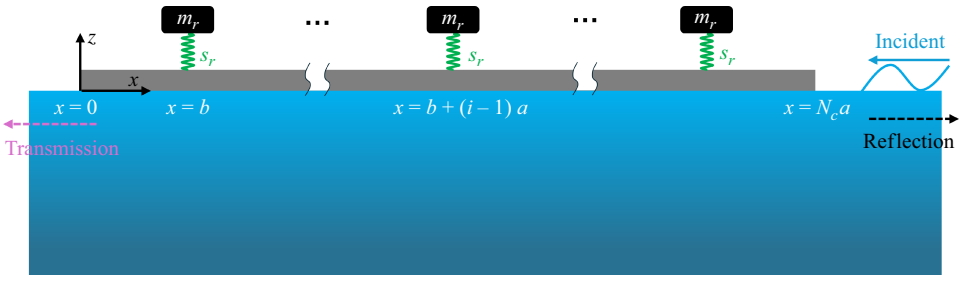


Figure 6. Schematic of a finite-size floating metaplate, consisting of N_c unit cells. Waves are incident from the positive x-direction. Resonators are located at $x = b + (i - 1)a$, where i ranges from 1 to N_c.

the right-hand side for $x > N_c a$ (labelled by subscript 'r', with incident and reflected waves). By considering all equations and conditions mentioned in § 2.1 and employing the eigenfunction matching method described in § 2.2, we obtain the velocity potential underneath the three parts as follows (Kohout *et al.* 2007; Meylan 2019; Iida & Umazume 2020):

$$\Phi(x, z, t) = Re\left[\frac{g}{\mathrm{i}\omega}\phi_{l,c,r}\mathrm{e}^{-\mathrm{i}\omega t}\right], \tag{4.1}$$

where

$$\phi_l(x, z) = \sum_{n=0}^{N} A_n \mathrm{e}^{\vartheta_n x}\varphi_n(z), \tag{4.2}$$

$$\phi_c^{(i)}(x, z) = \sum_{m=-2}^{M}\left[B_m^{(i)}\mathrm{e}^{\kappa_m x} + C_m^{(i)}\mathrm{e}^{-\kappa_m x}\right]\psi_m(z), \tag{4.3}$$

$$\phi_r(x, z) = \mathrm{e}^{\vartheta_0 x}\varphi_0(z) + \sum_{n=0}^{N} D_n \mathrm{e}^{-\vartheta_n x}\varphi_n(z). \tag{4.4}$$

Here, $\varphi_n(z)(n \geqslant 0)$ and $\psi_m(z)(m \geqslant -2)$ are given in (2.14) and (2.15), respectively; ϑ_n and κ_m are determined from (2.16) and (2.17); A_n, $B_m^{(i)}$, $C_m^{(i)}$ and D_n are unknown coefficients. In (4.3), the superscript (i) $(i = 1, 2, \cdots, N + 1)$ indicates the ith segment of the thin plate separated by the $(i - 1)$th and ith resonators on it. Specifically, for $i = 1$, $0 < x < b$; for $i = N_c + 1$, $b + (N_c - 1)a < x < N_c a$; and for any other i except 1 and $N_c + 1$, $b + (i - 2)a < x < b + (i - 1)a$. Note that (4.2) and (4.4) are obtained by taking into account the radiation conditions (Iida & Umazume 2020), which stipulate that the scattered waves (i.e. reflected and transmitted waves here) are outgoing to the infinite far field. In addition, the first term of (4.4) represents incident waves, i.e. $\Phi_I = Re[(g/\mathrm{i}\omega)\mathrm{e}^{\vartheta_0 x}\varphi_0(z)\mathrm{e}^{-\mathrm{i}\omega t}]$. The factor $g/\mathrm{i}\omega$ is a normalising value to unify the wave elevation of the free surface, which is calculated by the dynamic condition as

$$w = -\frac{1}{g}\frac{\partial \Phi}{\partial t}\bigg|_{z=0} = Re\left[\phi_{l,r}(x, 0)\mathrm{e}^{-\mathrm{i}\omega t}\right]. \tag{4.5}$$

And the harmonic deflection η of the plate (referring to (2.20)) can be written as

$$\eta^{(i)} = \frac{1}{-\mathrm{i}\omega}\frac{g}{\mathrm{i}\omega}\frac{\partial \phi_c^{(i)}}{\partial z}\bigg|_{z=0} \qquad i = 1, 2, \ldots, N_c + 1. \tag{4.6}$$

https://doi.org/10.1017/jfm.2025.10635 Published online by Cambridge University Press

Other physical quantities, such as the horizontal velocity of the fluid $\partial\phi/\partial x$, rotation angle $\partial\eta/\partial x$, bending moment $D\partial^2\eta/\partial x^2$ and shear force $-D\partial^3\eta/\partial x^3$ of the plate, can also be expressed by the velocity potential, as we did in § 2.

We use truncated summations of finite terms to approximate the solution of the velocity potential. According to (4.2)–(4.4), there are $(N+1)+2(M+3)\times(N_c+1)+(N+1)=2(N+1)+2(N_c+1)(M+3)$ unknowns in total. They are determined by matching and boundary conditions, which will be explained in the following.

First, we consider the matching conditions for the velocity potential and its normal derivative across the boundary between distinct regions underneath the free surface or plate segments. This implies that

$$\phi_I(0,z)=\phi_c^{(1)}(0,z), \tag{4.7}$$

$$\phi_c^{(i)}(b+(i-1)a,z)=\phi_c^{(i+1)}(b+(i-1)a,z)\quad(i=1,2,3,\ldots,N_c), \tag{4.8}$$

$$\phi_c^{(N_c+1)}(N_ca,z)=\phi_r(N_ca,z), \tag{4.9}$$

and

$$\left.\frac{\partial\phi_I}{\partial x}\right|_{x=0}=\left.\frac{\partial\phi_c^{(1)}}{\partial x}\right|_{x=0}, \tag{4.10}$$

$$\left.\frac{\partial\phi_c^{(i)}}{\partial x}\right|_{x=b+(i-1)a}=\left.\frac{\partial\phi_c^{(i+1)}}{\partial x}\right|_{x=b+(i-1)a}\quad(i=1,2,3,\ldots,N_c), \tag{4.11}$$

$$\left.\frac{\partial\phi_c^{(N_c+1)}}{\partial x}\right|_{x=N_ca}=\left.\frac{\partial\phi_r}{\partial x}\right|_{x=N_ca}. \tag{4.12}$$

The detailed forms of the matching conditions listed above are given in Appendix C. Following the approach used in § 2.3, we solve these equations by multiplying both sides by the vertical eigenfunction $\varphi_j(z)$ and integrating over the vertical domain from $z=-H$ to $z=0$. This process yields a total of $(N+1)\times[2(N_c+2)]$ equations, which are elaborated in Appendix C.

Then we consider the boundary and matching conditions for the plate. Free boundary conditions are set for the two ends of the plate, i.e. the bending moments and the shear forces at $x=0$ and $x=N_ca$ are zero. This implies that

$$\left.\frac{\partial^2\eta^{(1)}}{\partial x^2}\right|_{x=0}=0, \tag{4.13}$$

$$\left.\frac{\partial^3\eta^{(1)}}{\partial x^3}\right|_{x=0}=0, \tag{4.14}$$

and

$$\left.\frac{\partial^2\eta^{(N_C+1)}}{\partial x^2}\right|_{x=N_ca}=0, \tag{4.15}$$

$$\left.\frac{\partial^3\eta^{(N_c+1)}}{\partial x^3}\right|_{x=N_ca}=0. \tag{4.16}$$

At the point where the resonator is located (i.e. $x=b+(i-1)a$, $i=1,2,\ldots,N_c$), the deflection, the rotation angle and the bending moment of the plate are continuous, but there is a jump of force F in the shear force, where the dynamic force F was detailed in (2.38)–(2.40). This gives that

https://doi.org/10.1017/jfm.2025.10635 Published online by Cambridge University Press

$$\eta^{(i)}\Big|_{x=b+(i-1)a} = \eta^{(i+1)}\Big|_{x=b+(i-1)a}, \tag{4.17}$$

$$\frac{\partial \eta^{(i)}}{\partial x}\Big|_{x=b+(i-1)a} = \frac{\partial \eta^{(i+1)}}{\partial x}\Big|_{x=b+(i-1)a}, \tag{4.18}$$

$$D\frac{\partial^2 \eta^{(i)}}{\partial x^2}\Big|_{x=b+(i-1)a} = D\frac{\partial^2 \eta^{(i+1)}}{\partial x^2}\Big|_{x=b+(i-1)a}, \tag{4.19}$$

$$D\frac{\partial^3 \eta^{(i)}}{\partial x^3}\Big|_{x=b+(i-1)a} - D\frac{\partial^3 \eta^{(i+1)}}{\partial x^3}\Big|_{x=b+(i-1)a} = s_r \eta^{(i)}\Big|_{x=b+(i-1)a}\frac{-\tilde{\omega}^2}{1-\tilde{\omega}^2}, \tag{4.20}$$

where $i = 1, 2, \ldots, N_c$; $\tilde{\omega}$ can be found in (2.40). The detailed forms of (4.13)–(4.20) are also presented in Appendix C.

Finally, we get a total of $2(N+1)(N_c+2)+4+4N_c = (N_c+1)(2N+6)+2(N+1)$ equations. For the system to be well determined, this must exactly match the number of unknowns, $2(N+1)+2(N_c+1)(M+3)$. This condition is ensured by letting $M = N$.

4.2. *Time-domain response*

Using the procedure outlined above, the surface displacement in the frequency domain can be determined. The time-dependent solution is then obtained through superposition, leveraging the linearity of the system and applying the Fourier transform to transition from the frequency domain to the time domain. The surface displacement is a function of ω, therefore, we denote the complex frequency-domain surface displacement by $\eta(x, \omega)$. We assume that the incident wave is a Gaussian at $t = 0$. The time-dependent displacement is given by the following Fourier integral (Meylan 2019):

$$w(x, t) = Re\left\{\frac{1}{\pi}\int_0^{+\infty} \hat{f}(\omega)\eta(x, \omega)\mathrm{e}^{-\mathrm{i}\omega t}\mathrm{d}\omega\right\}, \tag{4.21}$$

where $\hat{f}(\omega)$ is

$$\hat{f}(\omega) = \sqrt{\frac{s}{\pi}}\mathrm{e}^{-s(\omega-\omega_c)^2}. \tag{4.22}$$

Here, s is a scaling factor that controls the overall width of the Gaussian wave packet, while ω_c represents the central frequency of the Gaussian.

4.3. *Numerical results*

We consider a finite-size floating metaplate consisting of $N_c = 30$ unit cells. All other parameters remain identical to those listed in table 1. In the following, we will first present the reflection and transmission coefficients obtained from the frequency-domain solutions for each individual incident frequency. Then, we will provide animations demonstrating the propagation and reflection of incident waves at various frequencies based on the time-domain results.

In the frequency-domain response analysis, the characteristics of reflection and transmission are evaluated based on the amplitude of the velocity potential in the far field from the plate. The reflection and transmission coefficients, R and T, are given as

$$R = D_0, \quad T = A_0, \tag{4.23}$$

which need to satisfy

$$|R|^2 + |T|^2 = 1, \tag{4.24}$$

as required by the energy conservation principle.

https://doi.org/10.1017/jfm.2025.10635 Published online by Cambridge University Press

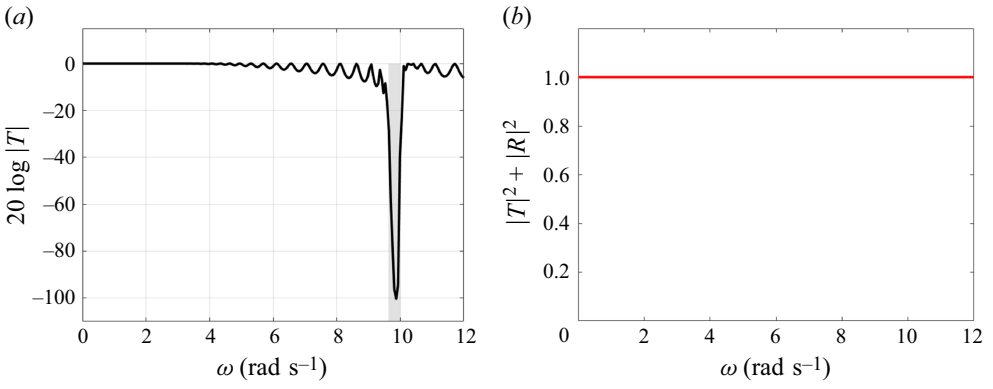


Figure 7. (*a*) Transmittance of the finite-size floating metaplate with resonant frequency $\omega_0 = 10\ \mathrm{rad\,s^{-1}}$. The grey shading indicates the locally resonant bandgap as shown in figure 3(*b*). (*b*) Value of $|T|^2 + |R|^2$ for verifying the law of conservation of energy.

Figure 7(*a*) illustrates the transmittance, $20 \log |T|$, of the finite-size floating metaplate as a function of the incident wave frequency ω. A sharp dip is observed within the grey-shaded frequency range, corresponding to the locally resonant bandgap identified in figure 3(*b*). This highlights the distinctive characteristic of the locally resonant bandgap, namely, its pronounced attenuation effect on incident waves within this frequency range. Figure 7(*b*) presents $|R|^2 + |T|^2$ as a function of ω, providing a clear verification of the energy conservation principle while also validating the accuracy and reliability of our numerical calculations.

On the other hand, the time-domain response results can provide a clearer demonstration of the blocking effect of the locally resonant bandgap on incident waves. We consider incident waves centred at different frequencies, corresponding to the passband below the bandgap, the stop band within the bandgap and the passband above the bandgap. The time-dependent responses for these three cases are shown as animations in Movies 1–3 which are given as supplementary material. From these results, we observe that for incident waves with a central frequency within the passbands (both below and above the bandgap), a significant portion of the wave energy propagates through the metaplate region. In contrast, for incident waves with a central frequency within the bandgap, almost all the energy is reflected. These results not only further validate our bandgap analysis but also highlight the potential of the floating metaplate as an effective water wave reflector.

5. Graded floating metaplate: broadband wave reflector with customisable working frequency range

Generally, the locally resonant bandgap exhibits a narrow width (Wu *et al.* 2021), that sometimes may be too small to be detectable (Skelton *et al.* 2018). To design a broadband wave reflector capable of working effectively in extremely challenging natural environments, the concept of a graded floating metaplate is introduced here. In classical wave systems (Cebrecos *et al.* 2014; Colombi *et al.* 2016; Bennetts *et al.* 2018; Wilks *et al.* 2022), graded design was widely employed for achieving the rainbow trapping or rainbow reflection effect, i.e. the spatial signal separation depending on frequency (Tsakmakidis, Boardman & Hess 2007). In this section, we demonstrate that a floating metaplate equipped with resonators featuring graded natural frequencies can exhibit a

https://doi.org/10.1017/jfm.2025.10635 Published online by Cambridge University Press

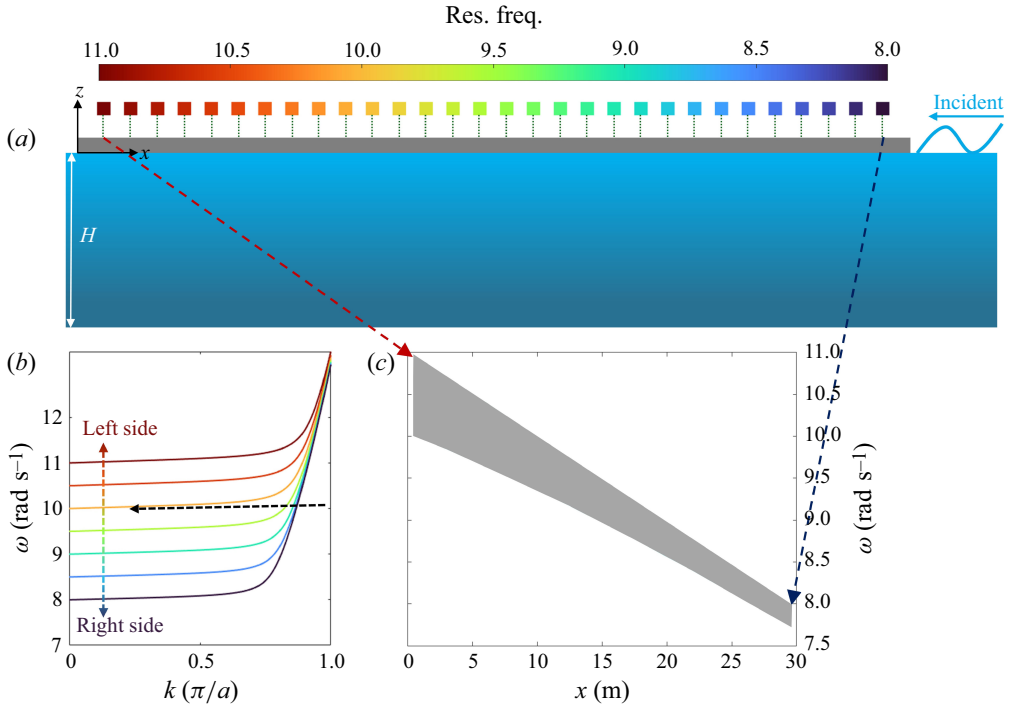


Figure 8. (*a*) Schematic representation of a graded floating metaplate, where the resonant frequencies of the attached resonators vary linearly from the left to the right side of the array and are rendered by different colours. (*b*) The second branch of dispersion curves for unit cells with different resonant frequencies for elucidating the rainbow reflection mechanism. The vertical arrow indicates that the band edge frequency gradually decreases from the left side to the right side, while the horizontal arrow represents an incident wave. (*c*) Evolution of the locally resonant bandgap as the resonant frequency decreases along the array.

pronounced rainbow reflection effect for surface water waves. More importantly, it can function as a broadband wave reflector, with its operating frequency range precisely tailored by the preset frequency range of the resonators, offering significant flexibility and performance customisability.

5.1. *Rainbow reflection mechanism for the graded metaplate*

We consider a finite-size metaplate consisting of $N_c = 30$ unit cells, where the resonant frequency ω_0 of the resonator mounted in each unit cell gradually increases linearly from 8 rad s^{-1} at the right end to 11 rad s^{-1} at the left end, as illustrated in figure 8(*a*). To enhance the practical feasibility of this set-up, we assume that the mass of the resonators remains constant, while the gradient variation in the resonant frequency of the resonators is achieved by altering the stiffness, i.e. s_r, of the springs connecting the resonators to the plate.

Unlike the conventional technique, which typically relies on the lower branch of the dispersion curve below the bandgap to achieve rainbow reflection (e.g. Bennetts *et al.* 2018; Wilks *et al.* 2022), here, we utilise the second branch of the dispersion curve located above the bandgap in the metaplate structure. This choice is motivated by two key factors. First, the second branch features a broad flat-band region (referring to figure 3*b*), which facilitates the phenomenon where different frequency components of the incident wave are effectively stopped at different positions within the structure. Second, as discussed in § 3.2, the lower edge of the second branch is precisely determined by the resonant frequencies

https://doi.org/10.1017/jfm.2025.10635 Published online by Cambridge University Press

of the resonators. This property enables highly customisable operating frequencies for the wave reflector, as will be elaborated later.

In order to reveal the rainbow reflection mechanism of this graded floating metaplate, the second branch of dispersion curves corresponding to the 1st, 5th, 10th, 15th, 20th, 25th and 30th unit cells are plotted together, as shown in figure 8(*b*). Considering an incident wave with a frequency of, for example, around 10 rad s^{-1}, indicated by the black dashed arrow, as it propagates from the right end of the host plate into the graded region, it can pass the first few unit cells since it lies within their passing band until it reaches the unit cell whose band edge corresponds to 10 rad s^{-1}. The wave modes are gradually transferred along the arrow from the dark blue curve to the yellow one, while the group velocity of the wave gradually decreases until it reaches zero. Then the wave will be stopped here, and, because the frequency of the incident wave is close to the resonant frequency of the resonator at that location, a significant portion of the incident wave energy will be transferred into the vibration of the resonator. This energy is subsequently converted into the bending vibration of the plate and reflected back. In general, incident waves of different frequencies reach zero group velocity at different unit cells. Since the lower edge of the flat band is precisely determined by the resonant frequency of the resonators, waves are stopped and reflected at the position where the resonant frequency of the local resonator matches or is close to the incident frequency (beyond this position, the waves enter the bandgap region, as shown in figure 8*c*), resulting in a spatial separation of incident water waves with different frequencies, akin to the effect of a rainbow. Besides, owing to the locally resonant mechanism, energy will be accumulated at the corresponding resonator, leading to the energy localisation in this resonator. This mechanism explains the reflection process of incident waves and provides an intuitive theoretical foundation for the implementation of a broadband water wave reflector discussed in the following sections.

5.2. *Frequency-domain response*

To demonstrate the rainbow reflection phenomenon, we perform a frequency response analysis on the graded metaplate. The numerical analysis procedure is almost the same as that described in § 4.1, with the exception that the boundary conditions related to the resonators must be modified to account for the fact that the resonant frequencies are no longer identical but gradually vary. This requires rewriting (4.20) as follows:

$$D\frac{\partial^3\eta^{(i)}}{\partial x^3}\Big|_{x=b+(i-1)a} - D\frac{\partial^3\eta^{(i+1)}}{\partial x^3}\Big|_{x=b+(i-1)a} = s_r^{(i)}\eta^{(i)}\Big|_{x=b+(i-1)a}\frac{-[\tilde{\omega}^{(i)}]^2}{1-[\tilde{\omega}^{(i)}]^2}, \tag{5.1}$$

where $i = 1, 2, \ldots, N_c$, $\tilde{\omega}^{(i)} = \omega/\omega_0^{(i)}$, in which $\omega_0^{(i)}$ is the value of the resonant frequency of the ith resonator (counting from the left end), and $s_r^{(i)} = m_r[\omega_0^{(i)}]^2$ is the spring stiffness of the ith resonator, where m_r is the mass of the resonator. In the numerical calculations, all other related parameters are consistent with those adopted in previous sections.

Figure 9 illustrates the amplitude of the reflection coefficient $|R|$ for the graded floating metaplate depicted in figure 8(*a*). The light cyan shaded region represents the frequency range of the resonant frequencies, which spans from 8 to 11 rad s^{-1}. It is evident that total wave reflection occurs for incident waves with frequencies within this range. This result is consistent with the previously explained rainbow effect: as the wave propagates along the metaplate, it reaches the resonator whose resonant frequency matches that of the incident wave, leading to reflection. Therefore, this graded floating metaplate can function as a 'broadband wave reflector', with its working frequency range entirely determined by the graded frequency range of the resonators.

https://doi.org/10.1017/jfm.2025.10635 Published online by Cambridge University Press

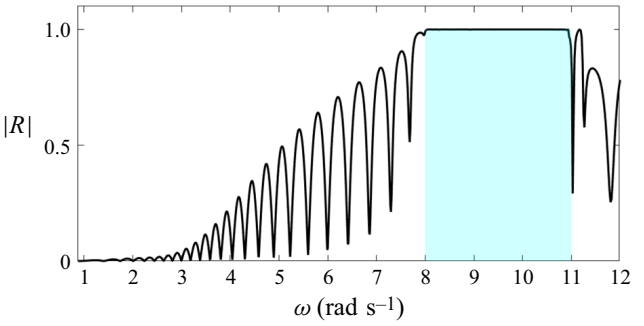


Figure 9. Amplitude of the reflection coefficient $|R|$ for the finite-size floating metaplate with the graded resonant frequencies ranging from 8 to 11 rad s^{-1}.

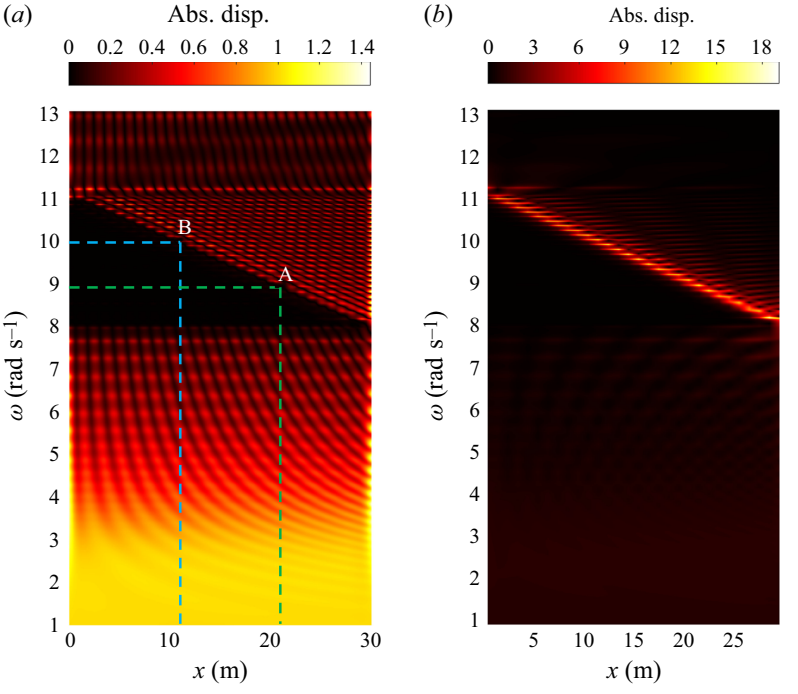


Figure 10. Displacement field of (*a*) the plate and (*b*) the resonators at different frequencies to demonstrate the rainbow reflection effect. In (*a*), A and B represent two specific cases where incident waves coming from the positive x-axis at different frequencies are completely stopped at distinct positions.

To illustrate the rainbow reflection and the broadband reflection phenomenon, figure 10 depicts the frequency response field for the graded metaplate. Figure 10(*a*) displays the normalised displacement field of the plate. The dark black triangular region indicates the behaviour within the graded resonant frequency range (8 to 11 rad s^{-1}), where the incident wave propagates a certain distance through the array before being stopped at a specific location. As the incident frequency ω increases linearly within this range, the stopping point shifts correspondingly in a linear manner, progressing from the right end toward the left end. Figure 10(*b*) illustrates the normalised absolute displacement of all resonators. One can observe that within the graded resonant frequency range of the resonators, the amplitudes of the resonators near the stopping point of the incident wave are significantly enhanced, and for different incident frequencies, the positions

https://doi.org/10.1017/jfm.2025.10635 Published online by Cambridge University Press

of the enhanced resonators vary accordingly. This unambiguously demonstrates the rainbow trapping effect. Moreover, it validates the previously described rainbow reflection mechanism, wherein the incident wave stops at a location where the resonant frequency of the local resonator matches the frequency of the incident wave and, subsequently, part of the wave's energy is converted into the vibration of the resonator.

5.3. *Time-dependent response*

Following the procedure outlined in § 4.2 and based on the frequency-domain response field given above, we now present the time-dependent response of the graded floating metaplate under the excitation of an incident wave centred at a specific frequency.

Figure 11 shows the results in the form of waterfall plots for the transient displacement field of the plate and resonators. For an incident Gaussian wave with central frequency $\omega_c = 9\,\mathrm{rad\,s^{-1}}$, it impinges into the right end of the plate ($x = 30\,\mathrm{m}$) and propagates to a position approximately one third of the plate's total length from the right end ($x \approx 20\,\mathrm{m}$). At this point, the group velocity of the wave decreases to zero, causing the wave to stop (see figure 11*b*). A portion of the incident wave's energy is then converted into the vibrational energy of the resonators near this location (see figure 11*c*). Over time, the wave is reflected back, and this back-scattering process repeats multiple times before gradually reaching a state of equilibrium. This continuous radiation of the wave signal is a characteristic phenomenon observed in rainbow structures, akin to the time spreading of reflected pulses in acoustics (Cebrecos *et al.* 2014). To visualise this result clearly, some snapshots of the time-dependent responses of the plate and resonators are presented in Appendix D, and the full animation can be found in Movie 4 as supplementary material. For comparison, figure 11(*d*,*e*,*f*) displays the results for an incident wave centred at $\omega_c = 10\,\mathrm{rad\,s^{-1}}$. In this case, the wave is trapped and reflected at a position approximately one third of the plate's total length from the left end ($x \approx 10\,\mathrm{m}$) (an animation illustrating this phenomenon is provided in Movie 5). These two cases align precisely with markers A and B in the frequency-domain wavefield shown in figure 10(*a*), which clearly indicates that rainbow reflection occurs around $x = 20\,\mathrm{m}$ and $x = 10\,\mathrm{m}$, respectively. In a nutshell, the characteristic behaviour of the rainbow trapping phenomenon manifests for incident waves centred at frequencies within the range of the resonant frequencies of the graded resonators, facilitating broadband total wave reflection.

To further substantiate our findings, we performed two additional time-domain simulations using broadband Gaussian wave packets. One with central frequency $\omega_c = 9.5\,\mathrm{rad\,s^{-1}}$, shown as figure 12(*a*), covers the entire frequency range of total reflection (i.e. 8–11 $\mathrm{rad\,s^{-1}}$). The corresponding time-domain displacement field of the water–metaplate–water region, as shown in figure 12(*c*), indicates that the packet is almost completely reflected, which confirms the broadband reflection of the graded floating metaplate. An animation illustrating this result is provided in Movie 6. The other one with spectrum centred at $8\,\mathrm{rad\,s^{-1}}$, as shown in figure 12(*b*), extends frequencies from 6 to 10 $\mathrm{rad\,s^{-1}}$, covering the range both inside and outside total reflection. From the time-domain displacement field shown in figure 12(*d*), it can be seen that a portion of the incident wave is transmitted through the metaplate, confirming that the waves with frequencies outside the total-reflection band cannot be blocked. The animation illustrating this phenomenon can be found in Movie 7.

5.4. *Customisable operating frequency range*

As previously mentioned, thanks to the fact that the upper bound (i.e. cutoff frequency of the graded structure) of the locally resonant bandgap is precisely determined by the resonant frequency of the resonators (see § 3.2), rainbow reflection occurs for incident waves

https://doi.org/10.1017/jfm.2025.10635 Published online by Cambridge University Press

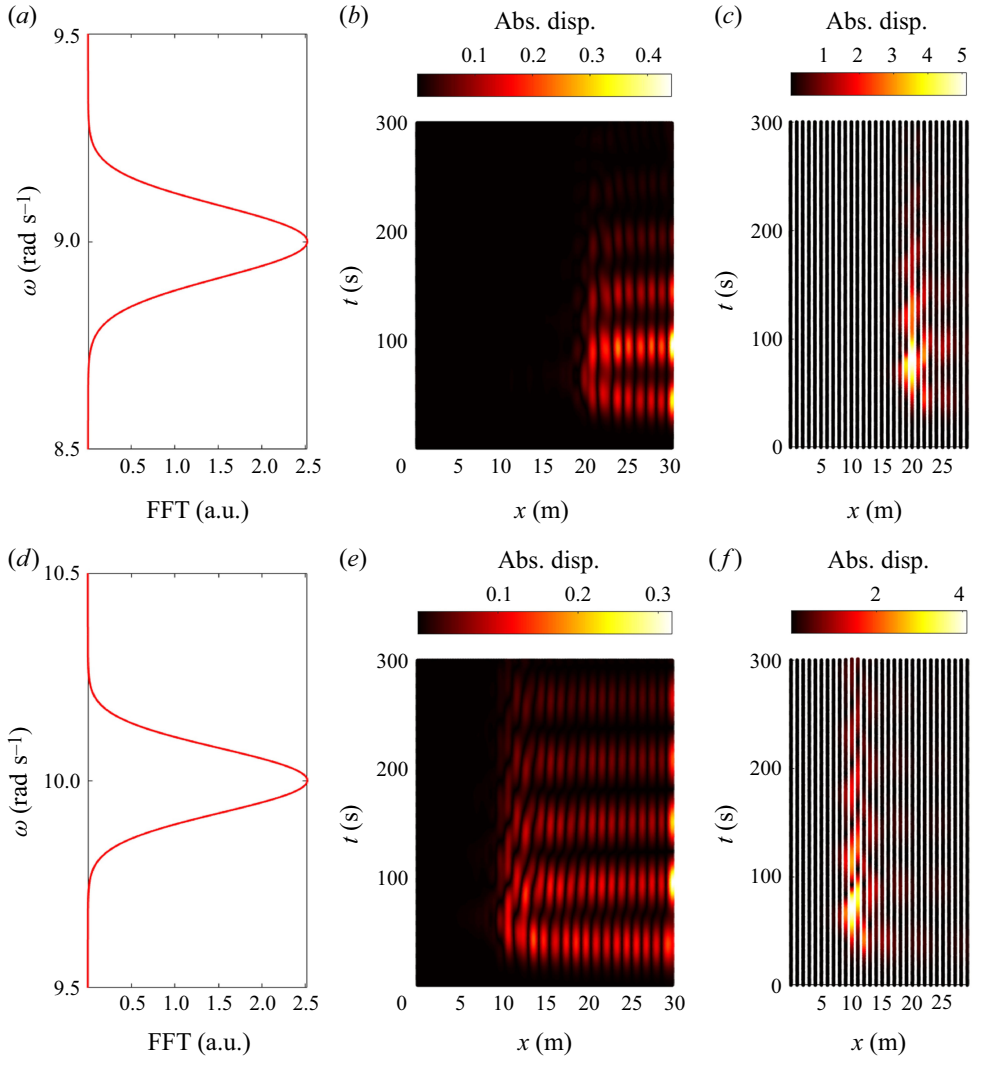


Figure 11. (*a*) An incident Gaussian wave centred at $\omega_c = 9$ rad s^{-1}, corresponding to marker A in figure 10(*a*). Waterfall plot representing the time-domain responses of (*b*) the plate and (*c*) the resonators to the incident Gaussian wave coming from the positive x-axis. Snapshots at some different times are shown in figure 14 in Appendix D. Panels (*d*), (*e*) and (*f*) are the same as (*a*), (*b*) and (*c*), respectively, except that now the incident wave is centred at $\omega_c = 10$ rad s^{-1}, corresponding to marker B in figure 10(*a*). Hereafter, 'FFT' refers to the magnitude of the fast Fourier transform of the Gaussian wave packet.

with central frequencies falling within the range that exactly matches the resonant frequency range of the graded resonators. In the following, we will briefly demonstrate that this frequency range, in which the graded-metaplate-enabled wave reflector operates, can be precisely customised by presetting the resonant frequency range of the graded resonators.

Now, we set the resonant frequency of the resonator to change, without the loss of generality, from 5 rad s^{-1} at the right-most end unit cell to 8 rad s^{-1} at the left-most end unit cell. Following the numerical procedure outlined previously, we obtain the reflection coefficient and the frequency-domain wavefield for this case, as shown in figure 13. One can clearly notice that the frequency range over which total reflection occurs (i.e. $|R| \to 1$)

https://doi.org/10.1017/jfm.2025.10635 Published online by Cambridge University Press

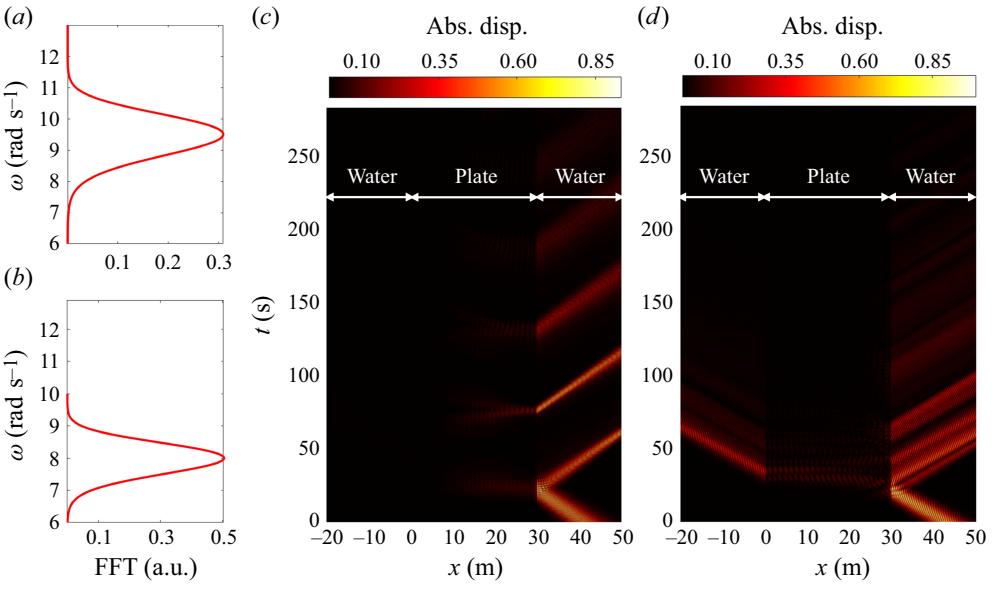


Figure 12. (*a*) A broadband Gaussian wave centred at $\omega_c = 9.5$ rad s^{-1}, covering the total-reflection frequency range. (*b*) A broadband Gaussian wave centred at $\omega_c = 8$ rad s^{-1}, spanning frequencies both inside and outside the range of total reflection. (*c*) Waterfall plot showing the time-domain responses of the water–metaplate–water region to the incident Gaussian wave in (*a*), coming from the positive x-axis. (*d*) Same as (*c*) but corresponding to the incident Gaussian wave in (*b*).

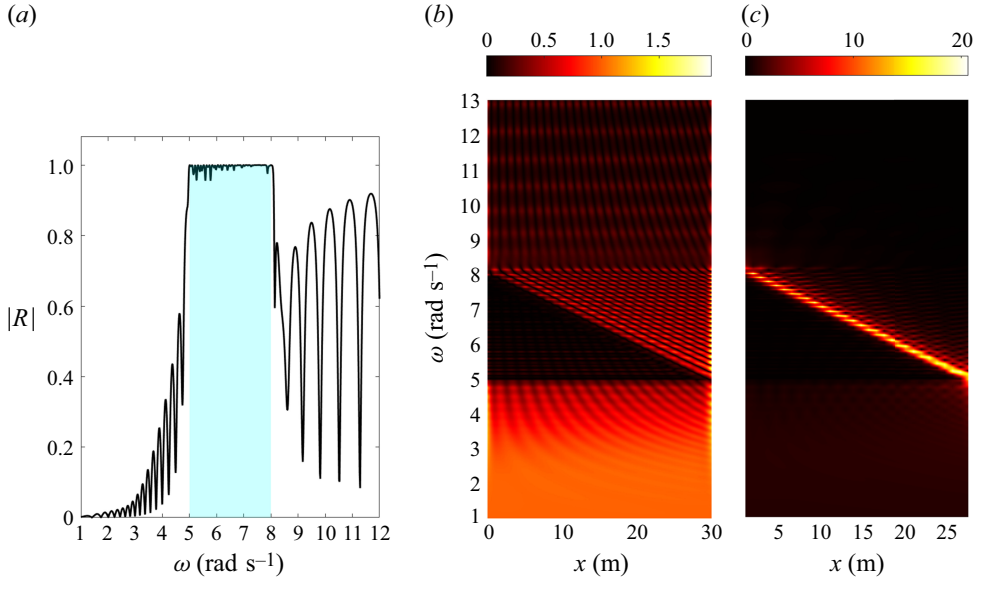


Figure 13. (*a*) Amplitude of the reflection coefficient $|R|$ for the finite-size floating metaplate with the graded resonant frequencies ranging from 5 to 8 rad s^{-1}. (*b*) Displacement field of the plate and (*c*) the resonators at different frequencies, illustrating the rainbow reflection effect. Panels (*b*) and (*c*) are the same as figure 10, execpt that the frequency range associated with the rainbow reflection shifted to the new frequency range of the graded resonators.

https://doi.org/10.1017/jfm.2025.10635 Published online by Cambridge University Press

shifts to the new frequency range of the graded resonators, as indicated by the light cyan region in figure 13(*a*). Once again, figures 13(*b*) and 13(*c*) illustrate that rainbow reflection is observed for incident waves with frequencies precisely within the resonant range of the resonators. In summary, the operating frequency range of this wave reflector, facilitated by the graded floating metaplate, can be accurately tuned by adjusting the predefined resonant frequency range of the resonators.

6. Conclusion

Inspired by the effective generation of low-frequency bandgaps by locally resonant metamaterials in acoustic and elastic waves, we systematically investigate the wave scattering by a floating plate decorated with local resonators. We obtain its band structure, and its exceptional capabilities in controlling surface gravity waves, such as achieving rainbow trapping and broadband wave reflection, are explored. Based on the linearised potential flow theory, the eigenfunction matching method and Bloch's theorem were applied to calculate the band structure of an infinitely periodic floating metaplate system. An effective model was proposed to analytically obtain the band structure, exhibiting good agreement with numerical results. The analytical model provides a clear description of the key features of the typical locally resonant bandgap. Additionally, the condition under which the analytical model is applicable was revealed through a direct error analysis. A numerical procedure was developed to analyse the wave interaction with the finite-sized floating metaplate. By utilising Fourier integration on the frequency-domain solutions, the time-domain responses were indirectly obtained, offering a more intuitive visualisation of the interaction phenomena between the floating metaplate and incoming surface waves. Furthermore, by designing the resonators on the metaplate with gradient variations in their resonant frequencies, we achieved rainbow trapping and reflection effects for incoming surface waves, thereby realising a broadband wave reflector. Most intriguingly, the operating frequency range of this reflector can be precisely determined by the resonant frequency range of the resonators on the plate. Although this work primarily serves as a proof-of-concept study, it offers valuable insights into the manipulation of water waves using metamaterials. These findings hold significant potential for applications in offshore industries, coastal structure protection engineering and the design of innovative wave energy converters.

Supplementary movies. Supplementary movies are available at https://doi.org/10.1017/jfm.2025.10635.

Funding. The authors gratefully acknowledge the support by King Abdullah University of Science and Technology (KAUST) Office of Sponsored Research (OSR) under Grant No. ORFS- CRG11-2022-5055, as well as KAUST Baseline Research Fund BAS/1/1626-01-01.

Declaration of interests. The authors report no conflict of interest.

Appendix A.

In (2.47), we used the assumption that $M = N$, $\boldsymbol{\mathcal{A}}$, $\boldsymbol{\mathcal{B}}$, $\boldsymbol{\mathcal{C}}$ and $\boldsymbol{\mathcal{D}}$ are all square matrices of dimension $2(M+3) \times 2(M+3)$, and can be respectively written as follows:

$$\boldsymbol{\mathcal{A}} = \left[\begin{array}{c|c} \boldsymbol{\mathcal{A}}_0 & \boldsymbol{\mathcal{A}}_0 \\ \boldsymbol{\mathcal{A}}_1 & -\boldsymbol{\mathcal{A}}_1 \\ \boldsymbol{a}_0 & \boldsymbol{a}_0 \\ \boldsymbol{a}_1 & -\boldsymbol{a}_1 \\ \boldsymbol{a}_2 & \boldsymbol{a}_2 \\ \boldsymbol{a}_3 & -\boldsymbol{a}_3 \end{array}\right], \quad \boldsymbol{\mathcal{B}} = \left[\begin{array}{c|c} -\boldsymbol{\mathcal{B}}_{0+} & -\boldsymbol{\mathcal{B}}_{0-} \\ -\boldsymbol{\mathcal{B}}_{1+} & \boldsymbol{\mathcal{B}}_{1-} \\ -\boldsymbol{b}_{0+} & -\boldsymbol{b}_{0-} \\ -\boldsymbol{b}_{1+} & \boldsymbol{b}_{1-} \\ -\boldsymbol{b}_{2+} & -\boldsymbol{b}_{2-} \\ -\boldsymbol{b}_{3+} & \boldsymbol{b}_{3-} \end{array}\right],$$

https://doi.org/10.1017/jfm.2025.10635 Published online by Cambridge University Press

$$\mathcal{C}=\left[\begin{array}{c|c} \boldsymbol{C}_{0+} & \boldsymbol{C}_{0-} \\ \boldsymbol{C}_{1+} & -\boldsymbol{C}_{1-} \\ \boldsymbol{c}_{0+} & \boldsymbol{c}_{0-} \\ \boldsymbol{c}_{1+} & -\boldsymbol{c}_{1-} \\ \boldsymbol{c}_{2+} & \boldsymbol{c}_{2-} \\ \boldsymbol{c}_{3+} & -\boldsymbol{c}_{3-} \end{array}\right], \quad \mathcal{D}=\left[\begin{array}{c|c} -\boldsymbol{\mathcal{D}}_{0+} & -\boldsymbol{\mathcal{D}}_{0-} \\ -\boldsymbol{\mathcal{D}}_{1+} & \boldsymbol{\mathcal{D}}_{1-} \\ -\boldsymbol{d}_{0+} & -\boldsymbol{d}_{0-} \\ -\boldsymbol{d}_{1+} & \boldsymbol{d}_{1-} \\ -\boldsymbol{d}_{2+} & -\boldsymbol{d}_{2-} \\ -\boldsymbol{d}_{3+} & \boldsymbol{d}_{3-} \end{array}\right]. \tag{A1}$$

Each of these matrices is formed by combining four submatrices (denoted by uppercase letters) and eight row vectors (denoted by lowercase letters). Each submatrix can be expressed as follows:

$$\begin{cases} \boldsymbol{\mathcal{A}}_0=\left[\begin{array}{cccc} P_{n=0,m=-2} & P_{n=0,m=-1} & \cdots & P_{n=0,m=M} \\ P_{n=1,m=-2} & P_{n=1,m=-1} & \cdots & P_{n=1,m=M} \\ \vdots & \vdots & \ddots & \vdots \\ P_{n=N,m=-2} & P_{n=N,m=-1} & \cdots & P_{n=N,m=M} \end{array}\right], \\ \text{where } P_{nm}=\int_{-H}^{0}\varphi_n(z)\psi_m(z)\,\mathrm{d}z \text{ (see 2.33)}, \\ \boldsymbol{\mathcal{A}}_1=\boldsymbol{\mathcal{A}}_0\,\mathrm{diag}(\kappa_{-2},\kappa_{-1},\cdots,\kappa_M), \\ \boldsymbol{\mathcal{B}}_{0+}=\boldsymbol{\mathcal{A}}_0\,\mathrm{diag}(\mathrm{e}^{\kappa_{-2}a},\mathrm{e}^{\kappa_{-1}a},\cdots,\mathrm{e}^{\kappa_M a}), \\ \boldsymbol{\mathcal{B}}_{0-}=\boldsymbol{\mathcal{A}}_0\,\mathrm{diag}(\mathrm{e}^{-\kappa_{-2}a},\mathrm{e}^{-\kappa_{-1}a},\cdots,\mathrm{e}^{-\kappa_M a}), \\ \boldsymbol{\mathcal{B}}_{1+}=\boldsymbol{\mathcal{B}}_{0+}\,\mathrm{diag}(\kappa_{-2},\kappa_{-1},\cdots,\kappa_M), \\ \boldsymbol{\mathcal{B}}_{1-}=\boldsymbol{\mathcal{B}}_{0-}\,\mathrm{diag}(\kappa_{-2},\kappa_{-1},\cdots,\kappa_M), \\ \boldsymbol{\mathcal{C}}_{0+}=\boldsymbol{\mathcal{A}}_0\,\mathrm{diag}(\mathrm{e}^{\kappa_{-2}b},\mathrm{e}^{\kappa_{-1}b},\cdots,\mathrm{e}^{\kappa_M b}), \\ \boldsymbol{\mathcal{C}}_{0-}=\boldsymbol{\mathcal{A}}_0\,\mathrm{diag}(\mathrm{e}^{-\kappa_{-2}b},\mathrm{e}^{-\kappa_{-1}b},\cdots,\mathrm{e}^{-\kappa_M b}), \\ \boldsymbol{\mathcal{C}}_{1+}=\boldsymbol{\mathcal{C}}_{0+}\,\mathrm{diag}(\kappa_{-2},\kappa_{-1},\cdots,\kappa_M), \\ \boldsymbol{\mathcal{C}}_{1-}=\boldsymbol{\mathcal{C}}_{0-}\,\mathrm{diag}(\kappa_{-2},\kappa_{-1},\cdots,\kappa_M), \\ \boldsymbol{\mathcal{D}}_{0+}=\boldsymbol{\mathcal{C}}_{0+},\ \boldsymbol{\mathcal{D}}_{0-}=\boldsymbol{\mathcal{C}}_{0-},\ \boldsymbol{\mathcal{D}}_{1+}=\boldsymbol{\mathcal{C}}_{1+},\ \boldsymbol{\mathcal{D}}_{1-}=\boldsymbol{\mathcal{C}}_{1-}, \end{cases} \tag{A2}$$

and for the row vectors, their mth element (m ranges from -2 to M) can be respectively described as

$$\begin{cases} \boldsymbol{a}_0^{(m)}=\dfrac{\mathrm{i}}{\omega}\dfrac{\alpha}{\beta\kappa_m^4+1-\gamma_0\alpha},\ \boldsymbol{a}_1^{(m)}=\dfrac{\mathrm{i}}{\omega}\dfrac{\alpha}{\beta\kappa_m^4+1-\gamma_0\alpha}\kappa_m, \\ \boldsymbol{a}_2^{(m)}=\dfrac{\mathrm{i}}{\omega}\dfrac{\alpha}{\beta\kappa_m^4+1-\gamma_0\alpha}\kappa_m^2,\ \boldsymbol{a}_3^{(m)}=\dfrac{\mathrm{i}}{\omega}\dfrac{\alpha}{\beta\kappa_m^4+1-\gamma_0\alpha}\kappa_m^3, \\ \boldsymbol{b}_{0\pm}^{(m)}=\dfrac{\mathrm{i}}{\omega}\dfrac{\alpha\mathrm{e}^{\pm\kappa_m a}}{\beta\kappa_m^4+1-\gamma_0\alpha},\ \boldsymbol{b}_{1\pm}^{(m)}=\dfrac{\mathrm{i}}{\omega}\dfrac{\alpha\mathrm{e}^{\pm\kappa_m a}}{\beta\kappa_m^4+1-\gamma_0\alpha}\kappa_m, \\ \boldsymbol{b}_{2\pm}^{(m)}=\dfrac{\mathrm{i}}{\omega}\dfrac{\alpha\mathrm{e}^{\pm\kappa_m a}}{\beta\kappa_m^4+1-\gamma_0\alpha}\kappa_m^2,\ \boldsymbol{b}_{3\pm}^{(m)}=\dfrac{\mathrm{i}}{\omega}\dfrac{\alpha\mathrm{e}^{\pm\kappa_m a}}{\beta\kappa_m^4+1-\gamma_0\alpha}\kappa_m^3, \\ \boldsymbol{c}_{0\pm}^{(m)}=\dfrac{\mathrm{i}}{\omega}\dfrac{\alpha\mathrm{e}^{\pm\kappa_m b}}{\beta\kappa_m^4+1-\gamma_0\alpha},\ \boldsymbol{c}_{1\pm}^{(m)}=\dfrac{\mathrm{i}}{\omega}\dfrac{\alpha\mathrm{e}^{\pm\kappa_m b}}{\beta\kappa_m^4+1-\gamma_0\alpha}\kappa_m, \\ \boldsymbol{c}_{2\pm}^{(m)}=\dfrac{\mathrm{i}}{\omega}\dfrac{\alpha\mathrm{e}^{\pm\kappa_m b}}{\beta\kappa_m^4+1-\gamma_0\alpha}\kappa_m^2,\ \boldsymbol{c}_{3\pm}^{(m)}=\dfrac{\mathrm{i}}{\omega}\dfrac{\alpha\mathrm{e}^{\pm\kappa_m b}}{\beta\kappa_m^4+1-\gamma_0\alpha}\left(\kappa_m^3\pm\dfrac{s_r}{D}\dfrac{\tilde{\omega}^2}{1-\tilde{\omega}^2}\right), \\ \boldsymbol{d}_{0\pm}^{(m)}=\boldsymbol{c}_{0\pm}^{(m)},\ \boldsymbol{d}_{1\pm}^{(m)}=\boldsymbol{c}_{1\pm}^{(m)},\ \boldsymbol{d}_{2\pm}^{(m)}=\boldsymbol{c}_{2\pm}^{(m)},\ \boldsymbol{d}_{3\pm}^{(m)}=\dfrac{\mathrm{i}}{\omega}\dfrac{\alpha\mathrm{e}^{\pm\kappa_m b}}{\beta\kappa_m^4+1-\gamma_0\alpha}\kappa_m^3. \end{cases} \tag{A3}$$

https://doi.org/10.1017/jfm.2025.10635 Published online by Cambridge University Press

Appendix B.

The dispersion relation (3.7) from the analytical model reads

$$\left\{\beta k^4+1-\left[\gamma_1\frac{1}{1-(\frac{\omega}{\omega_0})^2}+\gamma_0\right]\frac{\omega^2}{g}\right\}k\tanh kH=\frac{\omega^2}{g}. \tag{B1}$$

Solving for ω, we get two branches

$$\omega(k)=\begin{cases}\sqrt{\dfrac{\sigma_6+\sigma_5+\sigma_4+\sigma_3+\sigma_2+{\omega_0}^2}{\sigma_1}}, & \text{high branch, } \omega>\omega_0,\\ \sqrt{\dfrac{-\sigma_6+\sigma_5+\sigma_4+\sigma_3+\sigma_2+{\omega_0}^2}{\sigma_1}}, & \text{low branch, } \omega<\omega_0,\end{cases} \tag{B2}$$

where

$$\begin{aligned}&\sigma_1=2\left[\gamma_0\,k\tanh(kH)+1\right],\ \ \sigma_2=\gamma_1\,k\,{\omega_0}^2\tanh(kH),\ \ \sigma_3=\gamma_0\,k\,{\omega_0}^2\tanh(kH),\\ &\sigma_4=\beta\,g\,k^5\tanh(kH),\ \ \sigma_5=g\,k\tanh(kH),\ \ \sigma_6=\sqrt{\Sigma_6},\\ &\Sigma_6=\beta^2\,g^2\,k^{10}\,\sigma_7+2\,\beta\,g^2\,k^6\,\sigma_7-2\,\beta\,g\,\gamma_0\,k^6\,{\omega_0}^2\,\sigma_7+2\,\beta\,g\,\gamma_1\,k^6\,{\omega_0}^2\,\sigma_7\\ &\quad-2\,\beta\,g\,k^5\,{\omega_0}^2\tanh(kH)+g^2\,k^2\,\sigma_7-2\,g\,\gamma_0\,k^2\,{\omega_0}^2\,\sigma_7+2\,g\,\gamma_1\,k^2\,{\omega_0}^2\,\sigma_7\\ &\quad-2\,g\,k\,{\omega_0}^2\tanh(kH)+{\gamma_0}^2\,k^2\,{\omega_0}^4\,\sigma_7+2\,\gamma_0\,\gamma_1\,k^2\,{\omega_0}^4\,\sigma_7+2\,\gamma_0\,k\,{\omega_0}^4\tanh(kH)\\ &\quad+{\gamma_1}^2\,k^2\,{\omega_0}^4\,\sigma_7+2\,\gamma_1\,k\,{\omega_0}^4\tanh(kH)+{\omega_0}^4,\\ &\sigma_7=\tanh(kH)^2.\end{aligned} \tag{B3}$$

Appendix C.

Detailed forms of (4.7)–(4.12) are

$$\sum_{n=0}^{N}A_n\varphi_n(z)=\sum_{m=-2}^{M}\left[B_m^{(1)}+C_m^{(1)}\right]\psi_m(z), \tag{C1}$$

$$\begin{aligned}&\sum_{m=-2}^{M}\left[B_m^{(i)}\mathrm{e}^{\kappa_m[b+(i-1)a]}+C_m^{(i)}\mathrm{e}^{-\kappa_m[b+(i-1)a]}\right]\psi_m(z)\\ &=\sum_{m=-2}^{M}\left[B_m^{(i+1)}\mathrm{e}^{\kappa_m[b+(i-1)a]}+C_m^{(i+1)}\mathrm{e}^{-\kappa_m[b+(i-1)a]}\right]\psi_m(z),\ \ (i=1,2,\ldots,N_c),\end{aligned} \tag{C2}$$

$$\begin{aligned}&\sum_{m=-2}^{M}\left[B_m^{(N_c+1)}\mathrm{e}^{\kappa_m N_c a}+C_m^{(N_c+1)}\mathrm{e}^{-\kappa_m N_c a}\right]\psi_m(z)\\ &\quad=\mathrm{e}^{\vartheta_0 N_c a}\varphi_0(z)+\sum_{n=0}^{N}D_n\mathrm{e}^{-\vartheta_n N_c a}\varphi_n(z),\end{aligned} \tag{C3}$$

$$\sum_{n=0}^{N}A_n\vartheta_n\varphi_n(z)=\sum_{m=-2}^{M}\left[\kappa_m B_m^{(1)}-\kappa_m C_m^{(1)}\right]\psi_m(z), \tag{C4}$$

https://doi.org/10.1017/jfm.2025.10635 Published online by Cambridge University Press

$$\sum_{m=-2}^{M}\left[\kappa_m B_m^{(i)}\mathrm{e}^{\kappa_m[b+(i-1)a]}-\kappa_m C_m^{(i)}\mathrm{e}^{-\kappa_m[b+(i-1)a]}\right]\psi_m(z)$$
$$=\sum_{m=-2}^{M}\left[\kappa_m B_m^{(i+1)}\mathrm{e}^{\kappa_m[b+(i-1)a]}-\kappa_m C_m^{(i+1)}\mathrm{e}^{-\kappa_m[b+(i-1)a]}\right]\psi_m(z),\ (i=1,2,\ldots,N_c), \tag{C5}$$

$$\sum_{m=-2}^{M}\left[\kappa_m B_m^{(N_c+1)}\mathrm{e}^{\kappa_m N_c a}-\kappa_m C_m^{(N_c+1)}\mathrm{e}^{-\kappa_m N_c a}\right]\psi_m(z)$$
$$=\vartheta_0\mathrm{e}^{\vartheta_0 N_c a}\varphi_0(z)-\sum_{n=0}^{N}\vartheta_n D_n\mathrm{e}^{-\vartheta_n N_c a}\varphi_n(z). \tag{C6}$$

Multiplying both sides of these equations by the vertical eigenfunction $\varphi_j(z)$ and integrating from $z=-H$ to $z=0$, one can get (similar to (2.29)–(2.32))

$$A_j I_j=\sum_{m=-2}^{M}\left[B_m^{(1)}+C_m^{(1)}\right]P_{jm}, \tag{C7}$$

$$\sum_{m=-2}^{M}\left[B_m^{(i)}\mathrm{e}^{\kappa_m[b+(i-1)a]}+C_m^{(i)}\mathrm{e}^{-\kappa_m[b+(i-1)a]}\right]P_{jm}$$
$$=\sum_{m=-2}^{M}\left[B_m^{(i+1)}\mathrm{e}^{\kappa_m[b+(i-1)a]}+C_m^{(i+1)}\mathrm{e}^{-\kappa_m[b+(i-1)a]}\right]P_{jm},\ (i=1,2,\ldots,N_c), \tag{C8}$$

$$\sum_{m=-2}^{M}\left[B_m^{(N_c+1)}\mathrm{e}^{\kappa_m N_c a}+C_m^{(N_c+1)}\mathrm{e}^{-\kappa_m N_c a}\right]P_{jm}$$
$$=\mathrm{e}^{\vartheta_0 N_c a}I_0\delta_{0j}+\sum_{n=0}^{N}D_n\mathrm{e}^{-\vartheta_n N_c a}P_{jm}, \tag{C9}$$

$$A_j\vartheta_j I_j=\sum_{m=-2}^{M}\left[\kappa_m B_m^{(1)}-\kappa_m C_m^{(1)}\right]P_{jm}, \tag{C10}$$

$$\sum_{m=-2}^{M}\left[\kappa_m B_m^{(i)}\mathrm{e}^{\kappa_m[b+(i-1)a]}-\kappa_m C_m^{(i)}\mathrm{e}^{-\kappa_m[b+(i-1)a]}\right]P_{jm}$$
$$=\sum_{m=-2}^{M}\left[\kappa_m B_m^{(i+1)}\mathrm{e}^{\kappa_m[b+(i-1)a]}-\kappa_m C_m^{(i+1)}\mathrm{e}^{-\kappa_m[b+(i-1)a]}\right]P_{jm},\ (i=1,2,\ldots,N_c), \tag{C11}$$

$$\sum_{m=-2}^{M}\left[\kappa_m B_m^{(N_c+1)}\mathrm{e}^{\kappa_m N_c a}-\kappa_m C_m^{(N_c+1)}\mathrm{e}^{-\kappa_m N_c a}\right]P_{jm}$$
$$=\vartheta_0\mathrm{e}^{\vartheta_0 N_c a}I_0\delta_{0j}-\sum_{n=0}^{N}\vartheta_n D_n\mathrm{e}^{-\vartheta_n N_c a}P_{jm}, \tag{C12}$$

https://doi.org/10.1017/jfm.2025.10635 Published online by Cambridge University Press

where $0 \leqslant j \leqslant N$, the inner product of $\varphi_j(z)$ and $\varphi_n(z)$ reads

$$\int_{-H}^{0} \varphi_j(z)\varphi_n(z)\mathrm{d}z = I_j \delta_{nj}, \tag{C13}$$

where

$$I_j = \frac{H}{2\cos^2 \vartheta_j H} + \frac{\tan \vartheta_j H}{2\vartheta_j}, \tag{C14}$$

and P_{jm}, the inner product of $\varphi_j(z)$ and $\psi_m(z)$, is the same as P_{nm} in (2.33), except that the dummy n is replaced by j. Since j has $N+1$ different values, there are a total of $(N+1) \times [2(N_c+2)]$ equations here.

Detailed forms of (4.13)–(4.20) are

$$\sum_{m=-2}^{M} \frac{{\kappa_m}^2}{\beta\kappa_m^4 + 1 - \gamma_0\alpha}\left[B_m^{(1)} + C_m^{(1)}\right] = 0, \tag{C15}$$

$$\sum_{m=-2}^{M} \frac{{\kappa_m}^3}{\beta\kappa_m^4 + 1 - \gamma_0\alpha}\left[B_m^{(1)} - C_m^{(1)}\right] = 0, \tag{C16}$$

$$\sum_{m=-2}^{M} \frac{{\kappa_m}^2}{\beta\kappa_m^4 + 1 - \gamma_0\alpha}\left[B_m^{(N_c+1)}\mathrm{e}^{\kappa_m N_c a} + C_m^{(N_c+1)}\mathrm{e}^{-\kappa_m N_c a}\right] = 0, \tag{C17}$$

$$\sum_{m=-2}^{M} \frac{{\kappa_m}^3}{\beta\kappa_m^4 + 1 - \gamma_0\alpha}\left[B_m^{(N_c+1)}\mathrm{e}^{\kappa_m N_c a} - C_m^{(N_c+1)}\mathrm{e}^{-\kappa_m N_c a}\right] = 0, \tag{C18}$$

$$\sum_{m=-2}^{M} \frac{1}{\beta\kappa_m^4 + 1 - \gamma_0\alpha}\left\{B_m^{(i)}\mathrm{e}^{\kappa_m[b+(i-1)a]} + C_m^{(i)}\mathrm{e}^{-\kappa_m[b+(i-1)a]}\right\}$$
$$= \sum_{m=-2}^{M} \frac{1}{\beta\kappa_m^4 + 1 - \gamma_0\alpha}\left\{B_m^{(i+1)}\mathrm{e}^{\kappa_m[b+(i-1)a]} + C_m^{(i+1)}\mathrm{e}^{-\kappa_m[b+(i-1)a]}\right\}, \tag{C19}$$

$$\sum_{m=-2}^{M} \frac{\kappa_m}{\beta\kappa_m^4 + 1 - \gamma_0\alpha}\left\{B_m^{(i)}\mathrm{e}^{\kappa_m[b+(i-1)a]} - C_m^{(i)}\mathrm{e}^{-\kappa_m[b+(i-1)a]}\right\}$$
$$= \sum_{m=-2}^{M} \frac{\kappa_m}{\beta\kappa_m^4 + 1 - \gamma_0\alpha}\left\{B_m^{(i+1)}\mathrm{e}^{\kappa_m[b+(i-1)a]} - C_m^{(i+1)}\mathrm{e}^{-\kappa_m[b+(i-1)a]}\right\}, \tag{C20}$$

$$\sum_{m=-2}^{M} \frac{{\kappa_m}^2}{\beta\kappa_m^4 + 1 - \gamma_0\alpha}\left\{B_m^{(i)}\mathrm{e}^{\kappa_m[b+(i-1)a]} + C_m^{(i)}\mathrm{e}^{-\kappa_m[b+(i-1)a]}\right\}$$
$$= \sum_{m=-2}^{M} \frac{{\kappa_m}^2}{\beta\kappa_m^4 + 1 - \gamma_0\alpha}\left\{B_m^{(i+1)}\mathrm{e}^{\kappa_m[b+(i-1)a]} + C_m^{(i+1)}\mathrm{e}^{-\kappa_m[b+(i-1)a]}\right\}, \tag{C21}$$

$$\sum_{m=-2}^{M} \frac{1}{\beta\kappa_m^4 + 1 - \gamma_0\alpha}\left\{\left({\kappa_m}^3 + \frac{s_r}{D}\frac{\tilde{\omega^2}}{1-\tilde{\omega^2}}\right)B_m^{(i)}\mathrm{e}^{\kappa_m[b+(i-1)a]}\right.$$
$$\left. - \left({\kappa_m}^3 - \frac{s_r}{D}\frac{\tilde{\omega^2}}{1-\tilde{\omega^2}}\right)C_m^{(i)}\mathrm{e}^{-\kappa_m[b+(i-1)a]}\right\}$$

https://doi.org/10.1017/jfm.2025.10635 Published online by Cambridge University Press

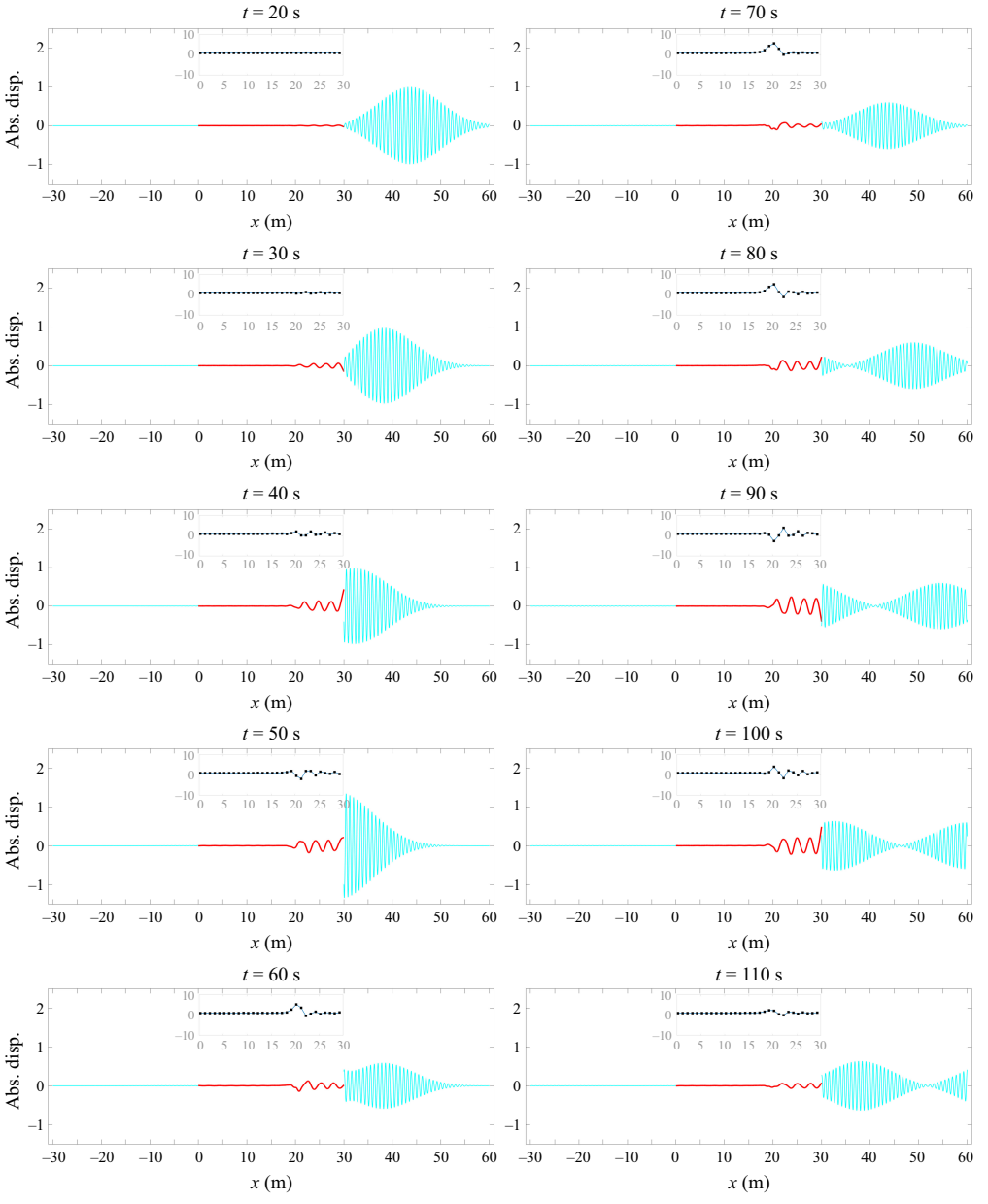


Figure 14. Snapshots of the time-dependent responses of a floating graded metaplate with the resonant frequency of the resonators varies from 8 at the right end to 11 rad s^{-1} at the left end. The incident wave is a Gaussian pulse centred at $\omega_c = 9$ rad s^{-1} with unit amplitude. The red line represents the plate while the black squares are the resonators. As time progresses, the incident wave is precisely halted at a position one third of the plate's total length from the right end and then reflected back (as illustrated in figure 11). The full animation can be found in Movie 4.

$$= \sum_{m=-2}^{M} \frac{{\kappa_m}^3}{\beta\kappa_m^4 + 1 - \gamma_0\alpha} \left\{ B_m^{(i+1)} \mathrm{e}^{\kappa_m[b+(i-1)a]} - C_m^{(i+1)} \mathrm{e}^{-\kappa_m[b+(i-1)a]} \right\}. \tag{C22}$$

In (C19)–(C22), i ranges from 1 to N_c, hence there are a total of $4 + 4N_c$ equations here.

https://doi.org/10.1017/jfm.2025.10635 Published online by Cambridge University Press

Appendix D.

To clearly visualise the time-dependent responses of the graded floating metaplate, as illustrated by the waterfall plots shown in figure 11, we provide movies in the supplementary material. Some snapshots from Movie 4 (considering an incident wave centred at $\omega_c = 9\,\mathrm{rad\,s^{-1}}$) are presented at different times in figure 14.

References

Archer, A.J., Wolgamot, H.A., Orszaghova, J., Bennetts, L.G., Peter, M.A. & Craster, R.V. 2020 Experimental realization of broadband control of water-wave-energy amplification in chirped arrays. *Phys. Rev. Fluids* **5** (6), 062801.

Balmforth, N.J. & Craster, R.V. 1999 Ocean waves and ice sheets. *J. Fluid Mech.* **395**, 89–124.

Bennetts, L G., Peter, M A. & Craster, R V. 2018 Graded resonator arrays for spatial frequency separation and amplification of water waves. *J. Fluid Mech.* **854**, R4.

Cebrecos, A., Picó, R., Sánchez-Morcillo, V.J., Staliunas, K., Romero-García, V. & Garcia-Raffi, L.M. 2014 Enhancement of sound by soft reflections in exponentially chirped crystals. *AIP Adv.* **4** (12), 124402.

Chen, Y., Hu, G. & Huang, G. 2017 A hybrid elastic metamaterial with negative mass density and tunable bending stiffness. *J. Mech. Phys. Solids* **105**, 179–198.

Chen, Y., Li, X., Nassar, H., Norris, A.N., Daraio, C. & Huang, G. 2019 Nonreciprocal wave propagation in a continuum-based metamaterial with space-time modulated resonators. *Phys. Rev. Appl.* **11** (6), 064052.

Chou, T. 1998 Band structure of surface flexural–gravity waves along periodic interfaces. *J. Fluid Mech.* **369**, 333–350.

Colombi, A., Colquitt, D., Roux, P., Guenneau, S. & Craster, R.V. 2016 A seismic metamaterial: the resonant metawedge. *Sci. Rep. UK* **6** (1), 27717.

Craster, R., Guenneau, S., Kadic, M. & Wegener, M. 2023 Mechanical metamaterials. *Rep. Prog. Phys.* **86** (9), 094501.

De Vita, F., De Lillo, F., Bosia, F. & Onorato, M. 2021 Attenuating surface gravity waves with mechanical metamaterials. *Phys. Fluids* **33** (4), 047113.

Euvé, L.-P., Pham, K. & Maurel, A. 2023 Negative refraction of water waves by hyperbolic metamaterials. *J. Fluid Mech.* **961**, A16.

Euvé L.-P., Pham K., Petitjeans P., Pagneux V. & Maurel A. 2024 Experimental demonstration of negative refraction of water waves using metamaterials with hyperbolic dispersion. *Phys. Rev. Fluids* **9** (11), L112801.

Farhat, M., Guenneau, S., Chen, P.-Y. & Wu, Y. 2021 Spacetime modulation in floating thin elastic plates. *Phys. Rev. B* **104** (1), 014308.

Fedele, F., Suryanarayana, P. & Yavari, A. 2023 On the effective dynamic mass of mechanical lattices with microstructure. *J. Mech. Phys. Solids* **179**, 105393.

Fox, C. & Squire, V.A. 1994 On the oblique reflexion and transmission of ocean waves at shore fast sea ice. *Phil. Trans. R. Soc. Lond. A: Phys. Engng Sci.* **347** (1682), 185–218.

Gusev, V.E. & Wright, O.B. 2014 Double-negative flexural acoustic metamaterial. *New J. Phys.* **16** (12), 123053.

Haberman, R. 2013 *Applied Partial Differential Equations with Fourier Series and Boundary Value Problems*, 5th edn. Pearson.

Hu, X., Chan, C.T., Ho, K.-M. & Zi, J. 2011 Negative effective gravity in water waves by periodic resonator arrays. *Phys. Rev. Lett.* **106** (17), 174501.

Huang, H.H., Sun, C.T. & Huang, G.L. 2009 On the negative effective mass density in acoustic metamaterials. *Intl J. Engng Sci.* **47** (4), 610–617.

Iida, T. & Umazume, K. 2020 Wave response of segmented floating plate and validation of its homogenized solution. *Appl. Ocean Res.* **97**, 102083.

Iida, T., Zareei, A. & Alam, M.-R. 2023 Water wave cloaking using a floating composite plate. *J. Fluid Mech.* **954**, A4.

Jin, Y., Pennec, Y., Bonello, B., Honarvar, H., Dobrzynski, L., Djafari-Rouhani, B. & Hussein, M.I. 2021 Physics of surface vibrational resonances: pillared phononic crystals, metamaterials, and metasurfaces. *Rep. Prog. Phys.* **84** (8), 086502.

Kohout, A.L., Meylan, M.H., Sakai, S., Hanai, K., Leman, P. & Brossard, D. 2007 Linear water wave propagation through multiple floating elastic plates of variable properties. *J. Fluids Struct.* **23** (4), 649–663.

https://doi.org/10.1017/jfm.2025.10635 Published online by Cambridge University Press

LAMB, H. 1997 On the vibrations of an elastic plate in contact with water. *Proc. R. Soc. Lond. A* **98** (690), 205–216.

LIANG, H., PORTER, R. & ZHENG, S. 2024 Wave scattering by plate array metacylinders of arbitrary cross-section. *J. Fluid Mech.* **1001**, A6.

LIU, Z., CHAN, C.T. & SHENG, P. 2005 Analytic model of phononic crystals with local resonances. *Phys. Rev. B* **71** (1), 014103.

LIU, Z., ZHANG, X., MAO, Y., ZHU, Y.Y., YANG, Z., CHAN, C.T. & SHENG, P. 2000 Locally resonant sonic materials. *Science* **289** (5485), 1734–1736.

LORENZO, M., PEZZUTTO, P., DE LILLO, F., VENTRELLA, F.M., DE VITA, F., BOSIA, F. & ONORATO, M. 2023 Attenuating surface gravity waves with an array of submerged resonators: an experimental study. *J. Fluid Mech.* **973**, A16.

LOUKOGEORGAKI, E. & KASHIWAGI, M. 2019 Minimization of drift force on a floating cylinder by optimizing the flexural rigidity of a concentric annular plate. *Appl. Ocean Res.* **85**, 136–150.

MA, G. & SHENG, P. 2016 Acoustic metamaterials: from local resonances to broad horizons. *Sci. Adv.* **2** (2), e1501595.

MCIVER, P. 2000 Water-wave propagation through an infinite array of cylindrical structures. *J. Fluid Mech.* **424**, 101–125.

MENG, Q.R. & LU, D.Q. 2017 Wave-induced hydrodynamic responses of a rigid body connected with elastic plates floating on a two-layer fluid. *J. Fluids Struct.* **68**, 295–309.

MEYLAN, M.H. 1997 The forced vibration of a thin plate floating on an infinite liquid. *J. Sound Vib.* **205** (5), 581–591.

MEYLAN, M.H. 2002 Spectral solution of time-dependent shallow water hydroelasticity. *J. Fluid Mech.* **454**, 387–402.

MEYLAN, M.H. 2019 The time-dependent vibration of forced floating elastic plates by eigenfunction matching in two and three dimensions. *Wave Motion* **88**, 21–33.

MICHELE, S., ZHENG, S., RENZI, E., BORTHWICK, A.G.L. & GREAVES, D.M. 2024*a* Hydroelastic theory for offshore floating plates of variable flexural rigidity. *J. Fluids Struct.* **125**, 104060.

MICHELE, S., ZHENG, S., RENZI, E., GUICHARD, J., BORTHWICK, A.G.L. & GREAVES, D.M. 2024*b* Wave energy extraction from rigid rectangular compound floating plates. *J. Fluids Struct.* **130**, 104193.

MIRANDA, E.J.P.JR., NOBREGA, E.D., RODRIGUES, S.F., ARANAS, C.JR., DOS SANTOS, J.M.C. 2020 Wave attenuation in elastic metamaterial thick plates: analytical, numerical and experimental investigations. *Intl J. Solids Struct.* **204-205**, 138–152.

MOLIN, B. 2001 On the added mass and damping of periodic arrays of fully or partially porous disks. *J. Fluids Struct.* **15** (2), 275–290.

PORTER, R. 2019 The coupling between ocean waves and rectangular ice sheets. *J. Fluids Struct.* **84**, 171–181.

RUPIN, M., LEMOULT, F., LEROSEY, G. & ROUX, P. 2014 Experimental demonstration of ordered and disordered multiresonant metamaterials for lamb waves. *Phys. Rev. Lett.* **112** (23), 234301.

SKELTON, E.A., CRASTER, R.V., COLOMBI, A. & COLQUITT, D.J. 2018 The multi-physics metawedge: graded arrays on fluid-loaded elastic plates and the mechanical analogues of rainbow trapping and mode conversion. *New J. Phys.* **20** (5), 053017.

SUGINO, C., RUZZENE, M. & ERTURK, A. 2020 An analytical framework for locally resonant piezoelectric metamaterial plates. *Intl J. Solids Struct.* **182-183**, 281–294.

TOKIĆ, G. & YUE, D.K.P. 2019 Hydrodynamics of periodic wave energy converter arrays. *J. Fluid Mech.* **862**, 34–74.

TORRENT, D., MAYOU, D. & SÁNCHEZ-DEHESA, J. 2013 Elastic analog of graphene: dirac cones and edge states for flexural waves in thin plates. *Phys. Rev. B* **87** (11), 115143.

TSAKMAKIDIS, K.L., BOARDMAN, A.D. & HESS, O. 2007 Trapped rainbow storage of light in metamaterials. *Nature* **450** (7168), 397–401.

WANG, K., ZHOU, J., CAI, C., XU, D. & OUYANG, H. 2019 Mathematical modeling and analysis of a meta-plate for very low-frequency band gap. *Appl. Math. Model.* **73**, 581–597.

WILKS, B., MONTIEL, F. & WAKES, S. 2022 Rainbow reflection and broadband energy absorption of water waves by graded arrays of vertical barriers. *J. Fluid Mech.* **941**, A26.

WU, L., WANG, Y., CHUANG, K., WU, F., WANG, Q., LIN, W. & JIANG, H. 2021 A brief review of dynamic mechanical metamaterials for mechanical energy manipulation. *Mater. Today* **44**, 168–193.

ZENG, J., ZHAO, X., SUN, X. & HU, X. 2023 Achieving complete band gaps of water waves with shallow-draft cylinder arrays. *Phys. Rev. Appl.* **19** (4), 044058.

ZHANG H., JIN H., ZHENG S. & XU D. 2024 Resonant periodic structures for strong attenuation of surface water wave. *J. Appl. Phys.* **135** (1), 014702.

https://doi.org/10.1017/jfm.2025.10635 Published online by Cambridge University Press

ZHANG, M. & SCHREIER, S. 2022 Review of wave interaction with continuous flexible floating structures. *Ocean Engng* **264**, 112404.

ZHENG, S., MEYLAN, M.H., ZHU, G., GREAVES, D. & IGLESIAS, G. 2020 Hydroelastic interaction between water waves and an array of circular floating porous elastic plates. *J. Fluid Mech.* **900**, A20.

ZHOU, X. & HU, G. 2009 Analytic model of elastic metamaterials with local resonances. *Phys. Rev. B* **79** (19), 195109.

ZHU, S., ZHAO, X., HAN, L., ZI, J., HU, X. & CHEN, H. 2024 Controlling water waves with artificial structures. *Nat. Rev. Phys.* **6** (4), 231–245.

https://doi.org/10.1017/jfm.2025.10635 Published online by Cambridge University Press